GEOPHYSICS, VOL. 77, NO. 3 (MAY-JUNE 2012); P. B107–B124, 19 FIGS., 1 TABLE.
10.1190/GEO2011-0243.1

Case History

Seismic velocity and attenuation structures of the Queen Charlotte Basin from full-waveform tomography of seismic reflection data

E. M. Takam Takougang[1] and A. J. Calvert[2]

ABSTRACT

We applied viscoacoustic waveform tomography to four seismic reflection lines from the central and northern part of the Queen Charlotte sedimentary basin and, using frequencies of 7–12 Hz, we estimated the compressional velocity and attenuation above a depth of approximately 1.2 km. We refined our previously published inversion strategy by alternating between phase-only and amplitude-plus-phase velocity inversion for the first two pairs of frequencies used, and added a second step, in which we inverted for attenuation from the lowest frequency using the final recovered velocity model and an initial homogeneous Q_P-model. Our recovered velocity and attenuation models demonstrated an overall good correlation with the available sonic and gamma-ray logs. Modeled seismic data matches the field data well and 1D velocity and attenuation profiles extracted at line intersections show a good correlation, thus demonstrating the robust nature of the results. Recovered velocities aid in interpreting shallow structures not readily identifiable on the conventional migration such as Quaternary strata and Pliocene faulting. Recovered attenuation values in the sedimentary rocks are generally consistent with saturated sandstones and consistent with the geology interpreted from well logs. Localized regions of elevated attenuation and associated low velocities correlate with siltstones and shales, the presence of hydrocarbons, or inferred increases in porosity due to fracturing. Seafloor pockmarks, where venting of gas occurs, are underlain by low velocities and an anomalous attenuation variation, and pipe-like gas chimneys are interpreted in two other areas of Hecate Strait. Igneous basement is associated with high velocity and high attenuation in its uppermost part, suggesting the presence of volcanic rocks, but the elevated attenuation may also be due to scattering and elastic mode conversions not included in the viscoacoustic inversion.

INTRODUCTION

The Queen Charlotte sedimentary basin (QCB) is the largest Tertiary basin on the west coast of Canada with an area of approximately 80,000 km^2 (500 km long and 150–200 km wide) (Whiticar et al., 2003). This large basin is bounded to the south and to the north by Vancouver Island and Alaska, respectively, and is terminated to the east by the Coast Plutonic Complex and to the west by the Queen Charlotte fault, which separates the North American plate from the Pacific plate (Woodsworth, 1991) (Figure 1). The QCB comprises up to 6 km of Tertiary sedimentary and volcanic fill above the igneous basement, and underlies Dixon Entrance, Hecate Strait, and Queen Charlotte Sound along the western margin of British Columbia (Rohr and Dietrich, 1992).

The geological structures of the QCB, their evolution as well as the hydrocarbon potential, have been thoroughly documented (e.g., Woodsworth, 1991; Rohr, 1992; Lyatsky, 1993; Whiticar, 2003). Information about the geology offshore has been obtained from eight petroleum-exploration wells drilled in the basin in the 1960s and from seismic reflection surveys, including one acquired in 1988 by the Geological Survey of Canada (GSC). In addition, many other geological and geophysical studies, including

Manuscript received by the Editor 4 July 2011; revised manuscript received 7 November 2011; published online 3 April 2012.
[1]Formerly Simon Fraser University, Department of Earth Sciences, Burnaby, British Columbia, Canada; presently Curtin University of Technology, Department of Exploration Geophysics, Perth, WA, Australia. E-mail: eta9@sfu.ca; takameric@gmail.com.
[2]Simon Fraser University, Department of Earth Sciences, Burnaby, British Columbia, Canada. E-mail: acalvert@sfu.ca.

high-resolution bathymetry and seafloor sampling, have been carried out in the basin (e.g., Irving et al., 2000; Halliday et al., 2008; Barrie et al., 2011).

The purpose of this work is to further the study of the basin by quantitatively imaging its upper structure using 2D viscoacoustic frequency domain full-waveform tomography applied to the limited offset seismic reflection data collected in 1988 by the GSC. P-wave velocities and inelastic attenuation models are derived from the inversion of four lines: 88-07, 88-06, 88-05 and 88-04 (Figure 1). These lines are located in Hecate Strait and partially Dixon Entrance. The expected depth of coverage is not more than 1200 m due to the limited maximum offset of the data (3770 m). The top 1200 m of the QCB contains Tertiary rocks of the Skonun and Masset formations, overlain by Quaternary rocks. The Skonun formation is composed of interbeded sandstones, shales, and siltstones, whereas the Masset formation consists mostly of basalts and volcaniclastic rocks (Dietrich, 1995).

Waveform tomography has the potential to effectively image subsurface structure in highly complex areas. It can therefore have a significant impact in the hydrocarbon industry, in which image distortions due to gas and complex geology have made the imaging process difficult using more conventional techniques. The high resolution of waveform tomography comes from the fact that all wave modes, which include diffractions, guided waves, reflection, and other scattering effects are taken into account during the inversion procedure. Unfortunately, the inclusion of all waveform modes has the consequence of increasing the nonlinearity of the inversion and the computational expense. The nonlinearity can be mitigated by a good starting model, careful preconditioning of the data, and the use of very low starting frequencies. When low starting frequencies are not available, an efficient inversion strategy must be selected to ensure sufficient convergence to the global minimum (e.g., Sirgue and Pratt, 2003 Takam Takougang and Calvert, 2010, 2011). Previous synthetic tests (e.g., Barnes and Charara, 2008; Brossier et al., 2009) have shown that acoustic waveform tomography can be effectively used with elastic data when the data are dominated by P-waves, and S-waves are of low amplitudes. This is the case in shallow marine environments such as the QCB, where S-waves and P-to-S conversions are weak due to the presence of soft sediments that imply a gradual change in S-wave velocity with depth and small velocity contrasts. However, the inversion might be more challenging on the eastern side of the basin where P-to-S-wave conversion is expected at the top of the shallow igneous basement, in addition to the seafloor.

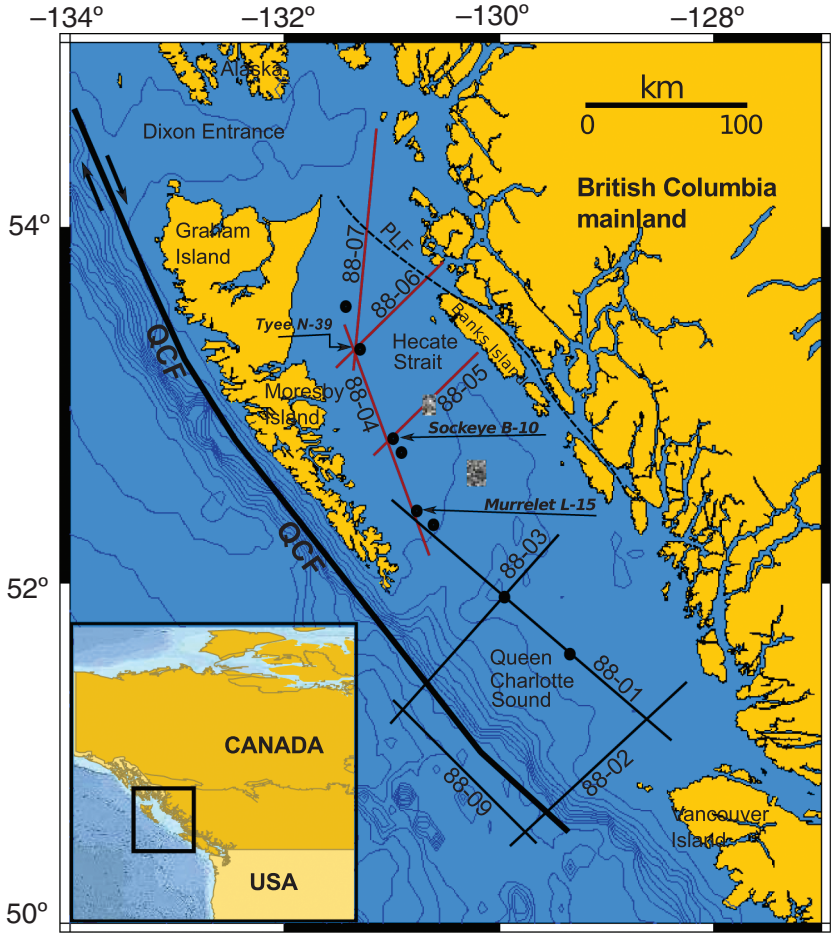

Figure 1. Location map of the Queen Charlotte Basin showing the seismic reflection lines acquired in 1988. The four lines used in this study are highlighted in red. The black dots indicate the location of wells. Wells Tyee N-39, Sockeye B-10, and Murrelet L-15 tie or are very close to the lines and were used for model assessment. The gray rectangles represent the study area of Halliday et al. (2008) (the big rectangle) and of Barrie et al. (2011) (the small rectangle) where pockmark structures were identified. QCF indicates the Queen Charlotte Fault and PLF is the Principe-Ladero Fault.

We begin by reviewing the geological setting of the basin, focusing on its history, structure, and stratigraphy. We then present the characteristics of the seismic survey, followed by the data preconditioning, and inversion strategy. The preconditioning of the data and inversion strategy (full-waveform tomography approach) was described in detail in Takam Takougang and Calvert (2011), referred to as paper 1. Therefore only a general review and some subsequent improvements to the methodology are provided here. The last part of the paper focuses on interpretation of the derived velocity and attenuation models. Our velocity perturbation models are also compared with conventional migrated sections from all the lines, and correlations between the velocity models, attenuation models, and sonic logs are presented to check the consistency of the results. A comparison is also made between the field data and the synthetic data derived from the recovered velocity and attenuation models.

GEOLOGICAL SETTING

The Queen Charlotte Basin (QCB) lies east of the Queen Charlotte fault which forms part of the Pacific-North America plate boundary. The basin's hydrocarbon potential is considered to be the greatest among the basins along the northwest margin of North America (Dietrich, 1995; Higgs, 1991). The geological history of the QCB is linked to the evolution of the Pacific continental margin and associated convergent and transcurrent plate interactions (Lewis et al., 1991; Rohr and Dietrich, 1992). The QCB first

developed during the Eocene over the Middle to late Triassic Wrangellia terrain which, with other parts of the Insular Belt, accreted to North America during the Middle Jurassic (Van der Heyden, 1992). The Insular Belt is the westernmost tectonic belt of the Canadian Cordillera. The northern section of the Insular Belt is separated from the Pacific plate by the dextral Queen Charlotte strike-slip fault.

There have been three successive phases of basin development: transtension, transform-margin, and transpression (Rohr and Dietrich, 1992; Irving et al., 2000). The transtensional phase started during the Eocene and lasted more than 25 million years. During this initial stage, most of the Miocene volcanics and associated sediments were deposited into an accommodation space associated with east–west crustal extension (Irving et al., 2000). During the pure transform phase of basin development, east–west extension ceased and igneous activity decreased and finally ceased. Subsidence continued during the Middle and Late Miocene, with continuous accumulation of sediments. The latest transpressional phase, which commenced in the latest Miocene or earliest Pliocene, was characterized by subsidence in the basin with relatively continuous sedimentary deposition. The relative plate motion became highly oblique and convergent, resulting in the uplift and erosion of the Queen Charlotte Islands (Irving et al., 2000).

Our area of study, the northern part of the basin, encompasses Hecate Strait and part of Dixon Entrance. Miocene structures in Hecate Strait are mainly oriented north–west, subparallel to the plate boundary. Converging and diverging fault segments are present, which result in a complex network of faults and subbasins, typically half-grabens bounded on their west side by a master fault. Dixon Entrance is underlain by a set of fault-bounded subbasins separated by basement platforms, which outcrop or lie close to the seafloor (Rohr and Dietrich, 1992).

Structure and stratigraphy

The QCB is underlain by Mesozoic and Tertiary volcanic, plutonic, and sedimentary rocks (Dietrich, 1995). The structure of the basin can be subdivided into three major sections from bottom to top:

1) *Lower Triassic–Lower Jurassic.* The igneous basement of the basin comprises volcanic rocks of the Triassic Karmutsen Formation, which are up to 4600 m thick (Dietrich, 1995). The Karmutsen strata are conformably overlain by up to 600 m of Upper Triassic and Lower Jurassic limestones, sandstones, and shales of the Kunga Group, and approximately 300 m of deep marine shale, siltstones, sandstones, and mudstones of the Lower Jurassic Maude Group. The Kunga and Maude Groups are considered to be the principal oil source rocks in the basin (Dietrich, 1995).
2) *Middle Jurassic–Cretaceous.* The Maude Group uncomformably underlies 800 m of volcanics and volcaniclastic rocks of the Middle Jurassic Yakoun and Moresby Groups, which lie uncomformably below up to 2500 m of Upper Jurassic-Cretaceous sandstone, shale, and conglomerate of the Longarm Formation and the Queen Charlotte Group. Middle Jurassic and older rocks are locally intruded by late Middle to Late Jurassic plutons. Upper parts of the Queen Charlotte Group locally contain volcanic rocks (Dietrich, 1995).
3) *Tertiary.* The Tertiary Formations are subdivided into Paleogene and Neogene strata. The Paleogene strata (Lower Tertiary) are 1000 m thick and comprises mostly volcanic flows with some conglomerates, black shale, and sandstones. The Neogene strata comprises volcanic and sedimentary rocks of, respectively, the Masset and the Skonun Formations. The Masset Formation comprises up to 4000 m of basalts, rhyolite flows, and pyroclastics (Dietrich, 1995). The Skonun Formation consists of interbedded sandstones, shales, conglomerates, and lignites (coals); and reaches a thickness of up to 6 km offshore. The Paleogene strata have limited reservoir quality, whereas the Masset Formation has good reservoir properties (Dietrich, 1995).
4) *Quaternary.* The Skonun and Masset Formations are unconformably overlain by the Quaternary Cape Ball Formation, which contains glacial and postglacial deposits. Glacial sediments are divided into three units: ice-contact tills, glaciomarine mud, and ice-distal mud to sandy-mud. This interpretation is based on surficial geology of the northwestern Canadian continental shelf, which includes the QCB (e.g., Luternauer et al., 1989; Barrie et al., 1991, 2006; Halliday et al., 2008).

SEISMIC REFLECTION SURVEYS

Eight regional 2D seismic reflection lines were acquired in 1988 by the GSC (Figure 1). These lines were shot offshore, using a 6358 in^3 air-gun array and recorded using a 240-channel hydrophone streamer with a minimum offset of 185 m and a maximum offset of 3770 m. The shot and receiver intervals were 45 and 15 m, respectively, and the shot and receiver depths were 12 m. A bandpass filter was applied before digitization: 8 Hz with a slope of 6 dB/octave to 90 Hz with a slope of 72 dB/octave. The four lines used for this study of Hecate Strait and partially Dixon Entrance are 88-04, 88-05, 88-06, and 88-07. Three exploration wells (Tyee N-39, Sockeye B-10, and Murrelet L-15) tie, or are very close to the intersection points of these seismic lines (Figure 1).

FULL-WAVEFORM TOMOGRAPHY

We used the 2D viscoacoustic, frequency-domain, waveform tomography approach as described in detail by Pratt et al. (1998), Pratt (1999), and Pratt and Shipp (1999). In essence, the objective of the inversion is to generate an update to a starting velocity and, when used, attenuation model, by iteratively minimizing the misfit between the forward modeled data and the field data, using the negative gradient. The gradient is computed by multiplying in the frequency domain the forward modeled wavefield by the backward-propagated data residual.

For a successful waveform inversion, the convergence criteria implies that the first arrival traveltimes calculated using the starting velocity model should match first arrivals from the field data to within half a cycle (Sirgue, 2003). Also, because we are using a 2D acoustic wave propagation scheme to model the 3D propagation of elastic data, amplitude correction is necessary, as well as the removal of elastic modes, such as ground roll or interface waves, not included in the acoustic wave propagation. The convergence criteria can be formulated mathematically using the traveltime error δt relative to the total arrival time T of the event as (Pratt, 2008)

$$\frac{\delta t}{T} \leq \frac{1}{2N_\lambda}, \tag{1}$$

where $N_\lambda = l/\lambda$ is a dimensionless term representing the propagation distance in terms of wavelengths and l is the propagation distance from the source to the receiver. Equation 1 shows that small values of N_λ are essential; they correspond to lower frequencies or, for a given frequency, to short-offset data. However, longer offset data are also essential because they are required to constrain the low wavenumbers in the velocity model (Sirgue and Pratt, 2004). When low frequencies are missing from the data, a specific inversion strategy is necessary in addition to a very good starting model.

The QCB survey is characterized by a relatively high starting frequency (7 Hz) and a limited maximum offset (3770 m), and we designed a specific strategy to improve convergence to a likely global minimum. This strategy also recovers structures to a depth of approximately 1200 m, which would not otherwise have been possible due to the amplitude distribution in the data. Early arrivals typically have larger amplitudes than late arrivals and thus dominate the gradient function, from which the velocity model update is calculated. Consequently, the shallow parts of the velocity model contribute more to the misfit function than deeper parts and are thus more accurately reconstructed. As mentioned in the "Introduction," a detailed description of this inversion strategy (full waveform tomography approach), as well as the preconditioning of the data are provided in paper 1. It should be noted that, unlike in paper 1, we applied waveform tomography to a maximum frequency of 12 Hz to reduce the computational cost because the four lines used in this study are longer, 93–154 km, whereas the line in paper 1, which had a length of 45 km, was inverted to a maximum frequency of 13.66 Hz. Below is a summary of the main steps involved:

Data preconditioning

The three main preconditioning steps of the four seismic lines are listed below:

1) *f-k filtering, trace editing, and lowpass filtering.* An f-k filter was used to remove steeply dipping coherent noise present in almost all the shot gathers. The data were then carefully inspected to remove bad traces and were finally lowpass filtered at 15 Hz to include only the frequencies necessary for the inversion.
2) *Shot-to-shot amplitude balancing and 2D amplitude scaling.* To balance the energy of each shot gather and, consequently, ensure a uniform model update along a seismic line during the inversion, amplitudes in each shot gather were normalized to the same maximum value. This normalization does not change the relative variation in amplitudes within individual traces, or the amplitude variation with offset. The data were then scaled to simulate 2D modeling by first multiplying every trace by $\sqrt{t}$, and second, by a scale factor obtained from a comparison of the logarithm of the root mean square (rms) amplitude variation with offset of the field and the modeled data. Finally, the data were muted 1.5 s after the first arrivals and a window of $T_w = 2$ s was used for the inversion.
3) *Data subsampling.* For lines 88-06, 88-05, and 88-07, the data were resampled to every second shot and every third receiver; this increases the shot interval to 90 m and the receiver interval to 45 m. For line 88-04, the shot interval was increased to every four shots giving a shot interval of 180 m, but the receiver interval remained equal to 45 m. This subsampling was carried out to reduce the computation time and to avoid oversampling because the maximum frequency used during the inversion is 12 Hz. These new geometries appear to be sufficient to avoid aliasing during waveform inversion, as discussed in paper 1.

Inversion strategy

The starting model for each of the four seismic lines was derived using traveltime inversion of first arrival traveltimes (Aldridge and Oldenburg, 1993). The initial model for traveltime inversion was calculated using a velocity gradient of 1.2 s^{-1} in the sediment and a velocity gradient of 2.5 s^{-1} to account for the transition from sedimentary to igneous rocks. The velocity of the water layer was kept constant at 1480 m^{-1}. Twenty iterations were computed for each line and an rms traveltime misfit of approximately 5.8 ms was obtained for lines 88-06, 88-04, and 88-07 and 3.6 ms for line 88-05. These results predicted the first arrival traveltimes to within half a cycle and respected the condition of equation 1 (see paper 1 for detailed explanations).

The waveform tomography inversion strategy consisted of successively recovering shallow to deep structures in the subsurface velocity and attenuation models (a layer-stripping approach). Shallow structures were recovered using near offset and early arrivals and deeper structures were recovered by additionally including far offsets and late arrivals. This was accomplished by weighting the gradient with depth and weighting the data residual with offset to focus on the region under reconstruction. Complex frequencies were used for the selection of time aperture in the frequency domain data. A complex angular frequency can be defined as (Mallick and Fraser, 1987; Pratt et al., 2004)

$$\omega = 2\pi f + i/\tau. \tag{2}$$

The imaginary component $1/\tau$ serves to dampen the contribution of late arrivals in the data residual, and thus enables the selection of time aperture in the frequency domain data. For the shallow and the deep reconstructions, two consecutive values of τ were used. These values correspond to $\tau = 0.8$ s and $\tau = 1.6$ s, which, respectively, represent 40% and 80% of the input data. Pairs of frequencies to include in the inversion were selected every $1/T_w = 0.5$ Hz from 7 to 12 Hz. For every pair of frequencies, five iterations were performed for each selected τ, making a total of 10 iterations for the shallow reconstruction and 10 iterations for the deep reconstruction (see Figure 2). The source signature was estimated as described in paper 1.

This inversion strategy was successfully applied in paper 1 to image a section of line 88-06. However, on line 88-05, we observed a lack of convergence in the inversion due to shadow zones in the input data, i.e., regions with very weak amplitudes. In those areas, the inversion has difficulty in recovering the correct phase of the data. For this reason, we refined our inversion strategy by alternating between phase-only and amplitude-plus-phase inversion for the low frequencies, i.e., frequencies ranging between 7 and 8.5 Hz. The phase-only inversion was performed with $\tau = 0.8$ and the amplitude-plus-phase inversion with $\tau = 1.6$. No change in the inversion strategy was made for the other frequencies. The phase-only inversion improves the recovery of the correct phase in shadow zones at early stages of the inversion.

We also refined the attenuation inversion strategy. Instead of introducing attenuation only at higher frequencies ($f \geq 10.5$ Hz), which produced a heterogeneous attenuation model due to the lack of low frequencies, we introduced attenuation from the starting frequency (7 Hz). We therefore performed a two-step inversion procedure: The first step consisted of inverting only for velocity from the lowest to the highest frequency, and the second step consisted of inverting for velocity and attenuation. During the second step, mostly the attenuation model was updated because a high-resolution velocity model had already been obtained from the first step. This strategy enables us to obtain a more laterally continuous attenuation model. The starting model for attenuation in all the lines was a homogeneous Q_P-model with $Q_P = 100$.

WAVEFORM TOMOGRAPHY RESULTS

The starting models and ray densities derived from first-arrival traveltime tomography are displayed in Figures 3 and 4. Velocity, attenuation, and perturbation velocity models derived using waveform tomography of lines 88-04, 88-05, 88-06, and 88-07 are displayed in Figures 5, 6, 7, and 8, respectively. The perturbation models (Figures 5c, 6c, 7c, and 8c) were obtained for every line

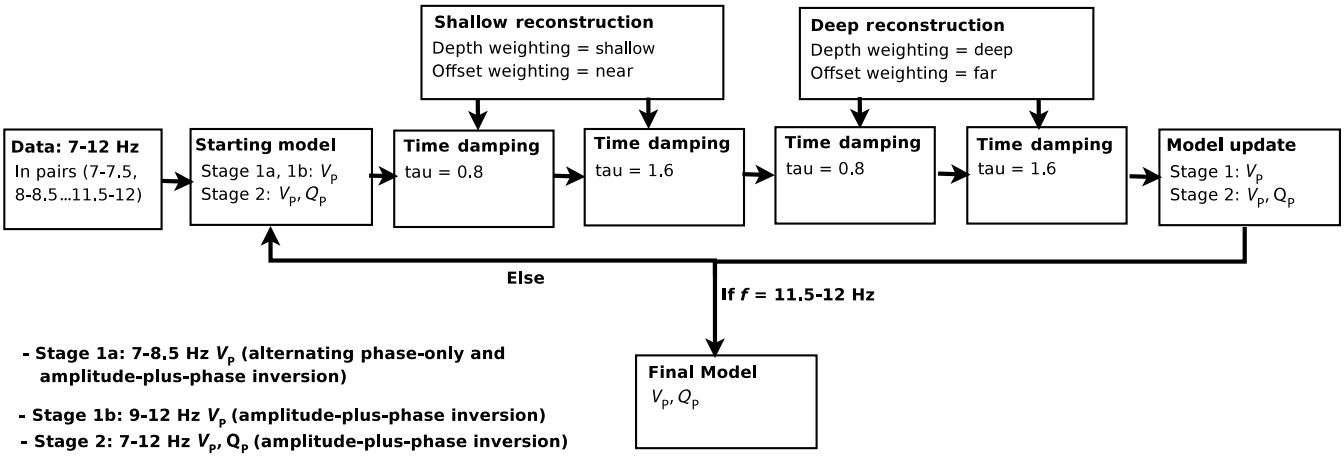

Figure 2. Schematic view of the inversion strategy used. The inversion is performed in two stages and the data are inverted in pairs from 7 to 12 Hz with a step length of 0.5 Hz. During stage 1, only velocities are inverted, and during stage 2, velocities and attenuation are inverted. For frequencies 7–8.5 Hz, phase-only, and amplitude-plus-phase inversion are performed successively for every pair of frequencies to improve the fitting (stage 1a).

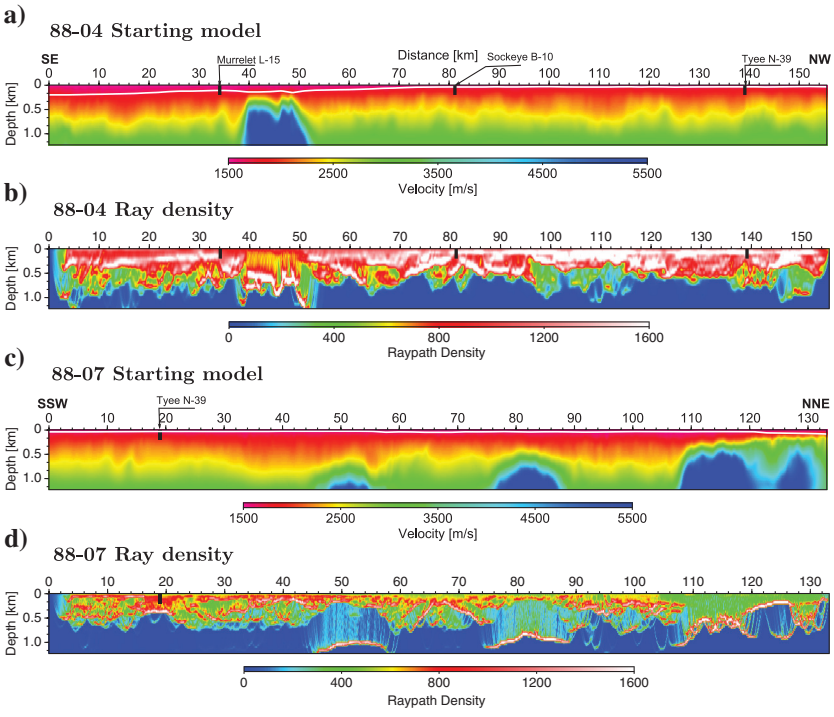

Figure 3. (a) Line 88-04 starting velocity model derived by first-arrival tomography and (b) associated ray density. (c) Line 88-07 starting velocity model derived by first-arrival tomography and (d) associated ray density. The ray coverage is limited to approximately 600-m depth but becomes deeper in igneous basement due to a greater velocity gradient in the initial velocity model. The white line represents the seafloor topography.

by subtracting the starting model from the final model and dividing the result by the starting model.

Generally, the results show two main geological features: the shallow sedimentary stratigraphy and basement of mostly Triassic igneous rocks (Rohr and Dietrich, 1992). The sedimentary rocks are characterized by velocities of approximately $1750 - 3000$ ms^{-1} and by attenuation of $Q_P^{-1} \leq 0.04$, with areas of attenuation as high as 0.15 (Figure 9a), whereas the basement rocks have velocities of $3500 - 5500$ ms^{-1} and inversion indicates attenuation generally between 0.01–0.07 (Figure 9b). Elevated attenuation ($Q_P^{-1} \geq 0.07$) is present mostly at the top of the igneous basement.

Model consistency

1D profiles at line intersections

The extracted 1D velocity profiles are generally similar at line intersections (Figure 10), thus showing the robustness of the inversion strategy selected. Small differences between various lines at the same well may be related to slight differences in the starting models used for the different lines. The extracted 1D attenuation profiles at the intersection of the lines are also generally similar (Figure 11), with the major horizons being consistently recovered in all the lines. However, it is clear that the attenuation results are not as robust as

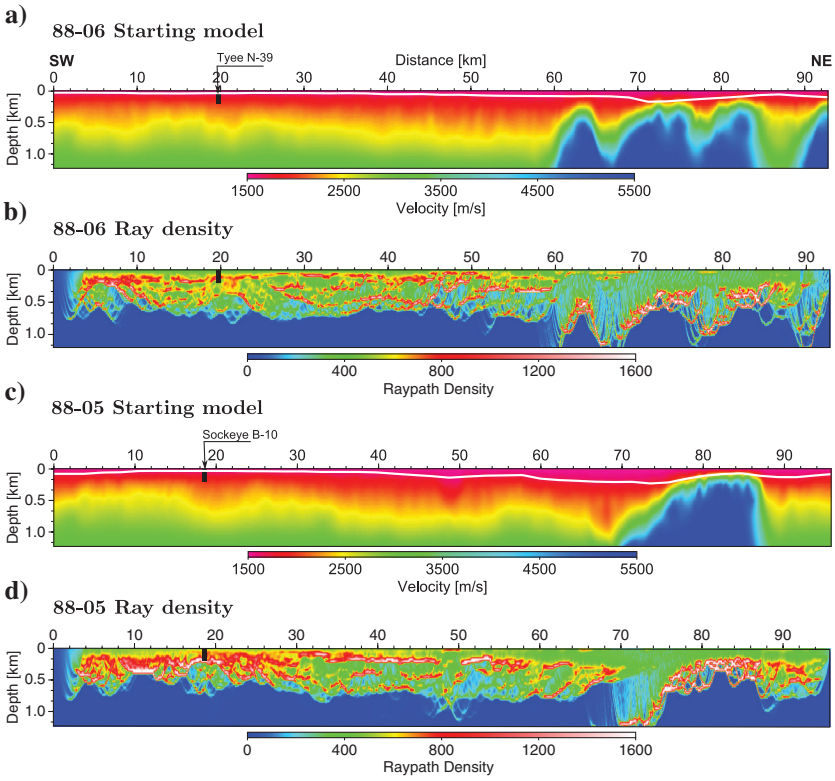

Figure 4. (a) Line 88-06 starting velocity model derived by first-arrival tomography and (b) associated ray density. (c) Line 88-05 starting velocity model derived by first-arrival tomography and (d) associated ray density. The ray coverage is limited to approximately 600-m depth but becomes deeper in igneous basement due to a greater velocity gradient in the initial velocity model. The white line represents the seafloor topography.

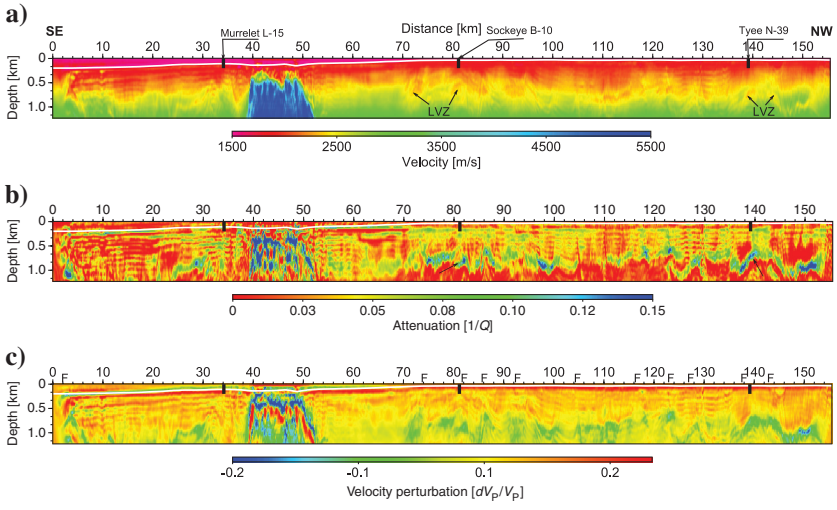

Figure 5. Line 88-04 waveform-tomography results. (a) Velocity model, (b) attenuation model, and (c) fractional velocity perturbation. Localized low-velocity zones (LVZ) and regions with interpreted shallow faulting (F) are indicated. Arrows in (b) indicate regions of high attenuation in sediment. The white line represents the seafloor topography.

those for velocity. Attenuation models mostly depend on the amplitudes of waveforms in contrast to the velocity models that mostly depend on arrival time and phases of the waveforms. Because many variable factors not related to attenuation, such as source and receiver coupling, coherent noise, and radiation patterns, affect the amplitude of waveforms, the inverted attenuation models are likely to exhibit greater variation than velocity models. Also, although we corrected the amplitudes of the 3D elastic input data to behave similar to 2D acoustic data, some differences may still persist and affect our estimate of attenuation. However, our recovered

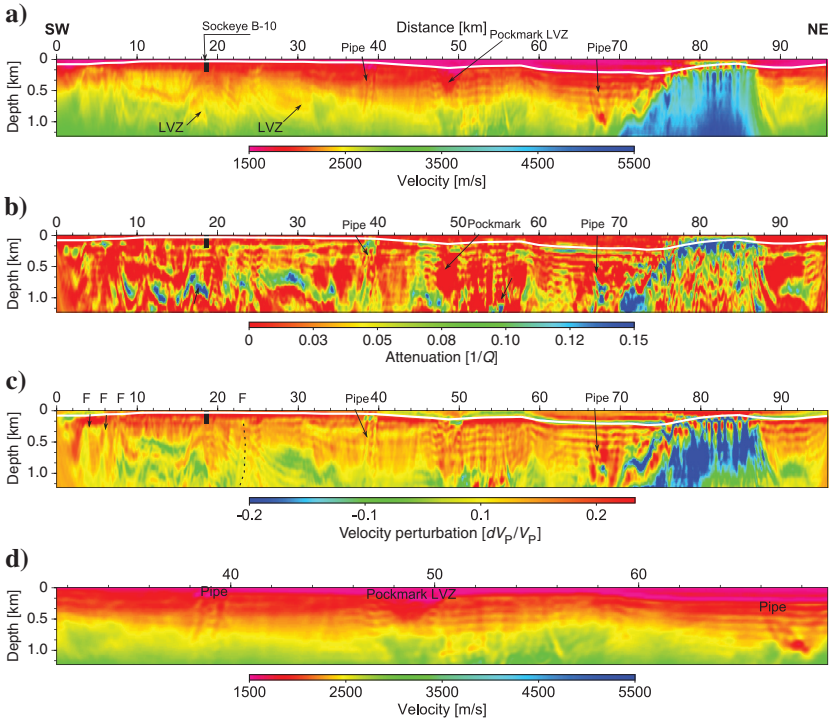

Figure 6. Line 88-05 waveform-tomography results. (a) Velocity model, (b) attenuation model, (c) fractional velocity perturbation, and (d) zoomed velocity model between $x = 31 - 69$ km to highlight the pockmark structures and interpreted pipe-like gas chimneys. Localized low-velocity zones (LVZ) and regions with interpreted shallow faulting (F) are indicated. Arrows in (b) indicate regions of high attenuation in sediment. Pipe-like gas chimneys are associated with low velocities and high attenuation. The white line represents the seafloor topography.

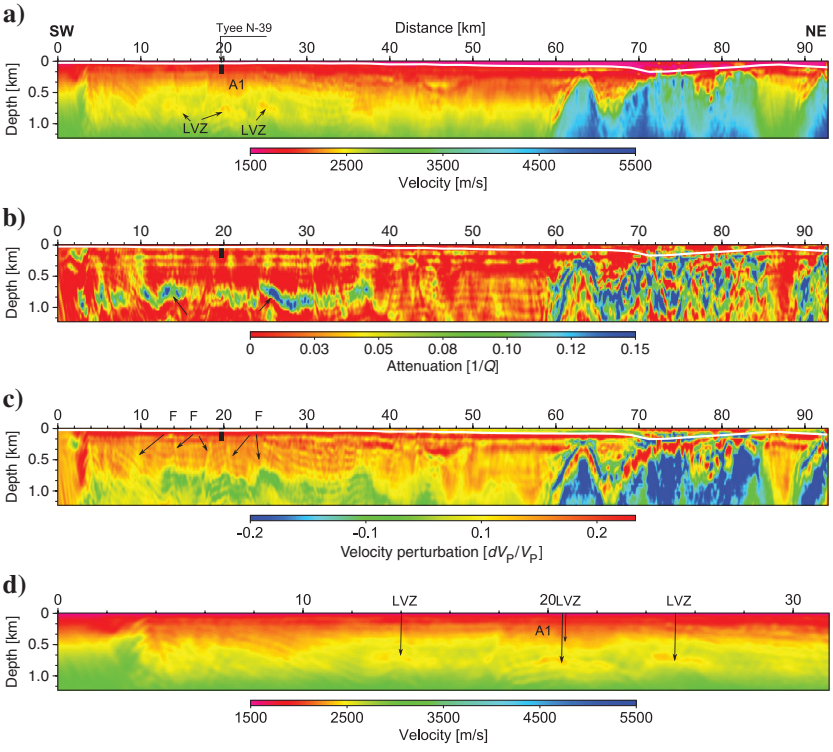

Figure 7. Line 88-06 waveform-tomography results. (a) Velocity model, (b) attenuation model, (c) fractional velocity perturbation, and (d) zoomed velocity model between $x = 0 - 32$ km. Localized low-velocity zones (LVZ), regions with interpreted shallow faulting (F) and antiform A1 are indicated. Arrows in (b) show regions with high attenuation in sediments and the white line represents the seafloor topography.

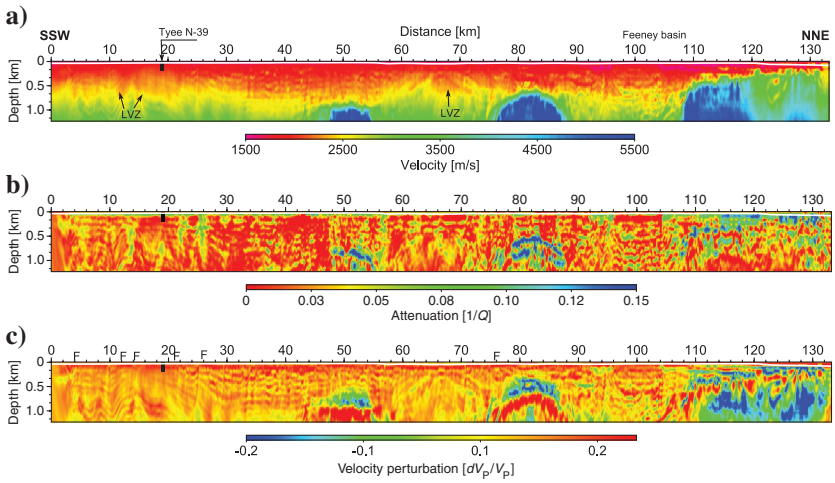

Figure 8. Line 88-07 waveform-tomography results. (a) Velocity model, (b) attenuation model, and (c) fractional velocity perturbation. Localized low-velocity zones (LVZ) and regions with interpreted shallow faulting (F) are indicated.

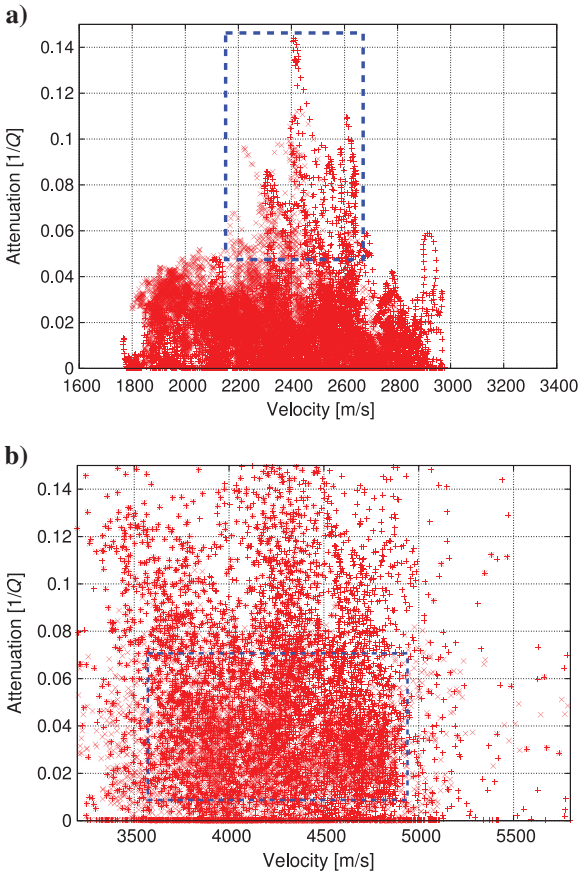

Figure 9. (a) Crossplotting of attenuation (Q_P^{-1}) versus velocity (V_P) in sedimentary rocks for all four seismic lines; velocities in sedimentary rocks ($1750 - 3000$ ms^{-1}) are generally associated with attenuation values $Q_P^{-1} \leq 0.04$. Elevated attenuation (≥ 0.05) is due to localized low-velocity zones. (b) Crossplotting of attenuation (Q_P^{-1}) versus velocity (V_P) at igneous basement; velocities at igneous basement ($3500 - 5000$ ms^{-1}) are associated with attenuation values $Q_P^{-1} = 0.01 - 0.07$, and attenuation as high as 0.1 is present mostly at top of basement.

attenuation models are more consistent than the attenuation model obtained in paper 1, using a section of line 88-06. This difference is due to the fact that in paper 1, we recovered the attenuation model starting from 10 Hz, whereas in this study, we recovered the attenuation models from the minimum frequency, 7 Hz. Therefore, these results show that a better estimate of attenuation can be obtained when low frequencies are available in the field data.

Synthetic modeling

Synthetic and field data are also used to check the reliability of the results. Synthetic data were obtained after forward modeling in the frequency domain using the velocity and attenuation models from waveform tomography at 12 Hz, and the results are compared using a true-amplitude display with the field data in a common offset gather corresponding to an offset of 2.915 km. Comparison in the common offset domain has the advantage of clearly showing the match along the entire line. Only the comparisons for lines 88-05 and 88-06 are shown (Figures 12 and 13), but similar results were obtained for the remaining lines. In the sedimentary section, the arrival times, the waveform shapes of the first and late arrivals within the 2 s window, and the amplitude variations are well reproduced in the synthetic data, between receiver locations 0–57 km on line 88-06 and between 0–67 km and 86–92 km on line 88-05. Diffraction patterns are well reproduced at receiver locations 50–56 km on line 88-05 and at 40–46 km on line 88-06. Shadow zones, i.e., areas with weak amplitudes in the sedimentary section, are also well reproduced at 0–5 km and 40–46 km on line 88-05 (Figure 12a and 12b). Just below the seafloor, the delayed arrivals centered at 48 km and the overlaying shadow zone at 40–46 km on line 88-05 are also well reproduced in the synthetic data using a nearer offset of 2.015 km (Figure 12c and 12d). Where the igneous basement is shallow, i.e., at 58–88 km on line 88-06 and 70–86 km on line 88-05, the match between synthetic and field data is poor. For example, late arrivals at 64–66 km and 74–78 km on line 88-06 are not well reproduced in the synthetic data. This is not a surprising result because P-waves propagating in this area are strongly attenuated, partially due to heterogeneity, but amplitudes are also reduced by S-wave conversion, which is not included in the inversion. Converted S-waves are expected to be stronger in this area due to the greater velocity contrast between low-velocity sedimentary and high-velocity igneous rocks.

Well ties

Sonic logs

To assess the quality of the waveform tomography results, a comparison was made between the available sonic logs and 1D velocity profiles extracted from the seismic lines. Three seismic lines, 88-04, 88-06, and 88-07, intersect near the Tyee N-39 well. One-dimensional velocity profiles were extracted from the starting and final velocity models and superimposed on the sonic log from the well (Figure 14). A generally good match exists between the sonic log and the 12 Hz final models, showing the reliability of the results.

The most impressive result is obtained with line 88-06 (Figure 14a) in which the Pliocene/upper-Miocene unconformity is characterized by a decrease in velocity, and the presence of coal at 660 m is well resolved. This match is actually better than the one obtained in paper 1, where a 50-m offset was observed between the sonic log and the final velocity profile near the unconformity; this improvement is explained by the changes made to the inversion strategy. A mismatch is, however, evident at 1100 m where an increase in velocity of approximately 200 ms^{-1} is observed. On lines 88-04 and 88-07 (Figure 14b and 14c), the low-velocity layer at 550–600 m is well resolved, but the underlying higher-velocity layer at 600–660 m is not fully recovered. These mismatches may be related to anisotropy or to the increase in nonlinearity in the inversion, whereas small changes in layer thickness and velocity can have a disproportionate effect on the data, leading to convergence problems Pratt et al., 2004).

The Sockeye B-10 and the Murrelet L-15 wells were superimposed on the velocity models from lines 88-05 and 88-04, respectively (Figure 14d, 14e, and 14f). A generally good match exists between the Murrelet L-15 sonic and line 88-04 where the starting 1D velocity profile matched the sonic velocities well. The tie of the Sockeye B-10 sonic log with line 88-05 (Figure 14d) and line 88-04 (Figure 14e) shows a good recovery of the decrease in velocity at 950 m, associated with oil staining, but there are mismatches at 200–750 m on line 88-05, with velocities from the 1D profile faster than the sonic velocities and an unexplained increase in velocity at 400–550 m in the 1D profile from line 88-04. The Sockeye B-10 well, however, does not exactly tie to lines 88-05, and 88-04 and the location of the well was projected to the nearest points on the respective lines where the 1D profiles were extracted. The Sockeye B-10 well is approximately 2 km from line 88-04 and 0.5 km from line 88-05. In contrast, the Tyee N-39 well is only 0.2 km from line 88-06. Consequently, the mismatches observed between the sonic velocity of the Sockeye B-10 well and the 1D velocity profiles from lines 88-04 and 88-05 may be related to differences in geological structure between the well location and the projected location on the lines. In all cases, the final 7–12 Hz waveform tomography model fit the sonic log better than the starting model from traveltime tomography.

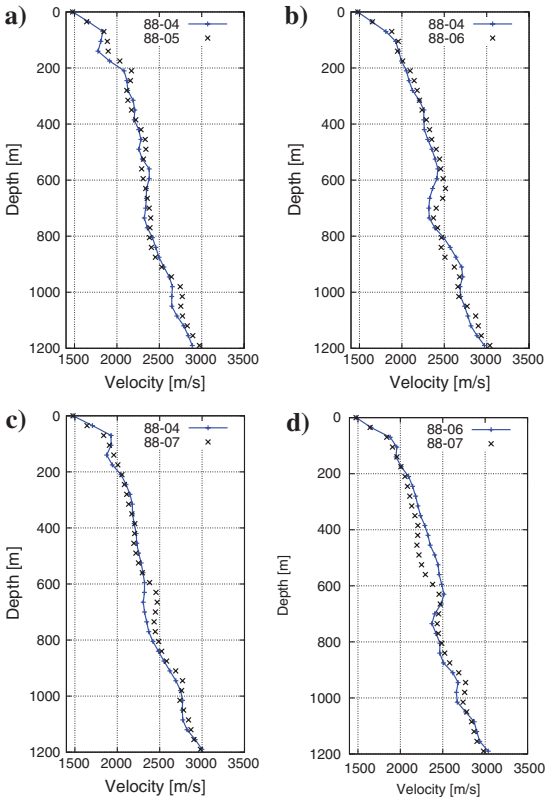

Figure 10. One-dimensional profiles of waveform tomography velocity models at the intersection between (a) line 88-04 and line 88-05, (b) line 88-04 and line 88-06, (c) line 88-04 and line 88-07, and (d) line 88-06 and line 88-07. The good agreement between various profiles at the intersection of lines shows the robustness of the inversion strategy.

Estimated clay content

Intrinsic seismic attenuation can potentially predict rock properties such as porosity, permeability, and clay content. A relationship linking attenuation (Q_P^{-1}) and clay content in sandstones was shown by Klimentos and McCann (1990), and can be written as

$$Q_P = 179C^{-0.843}, \tag{3}$$

where C is the percent clay content by volume. We used this relationship (equation 3) to estimate the percentage of clay content in the sedimentary rocks at two well locations, where siltstones and

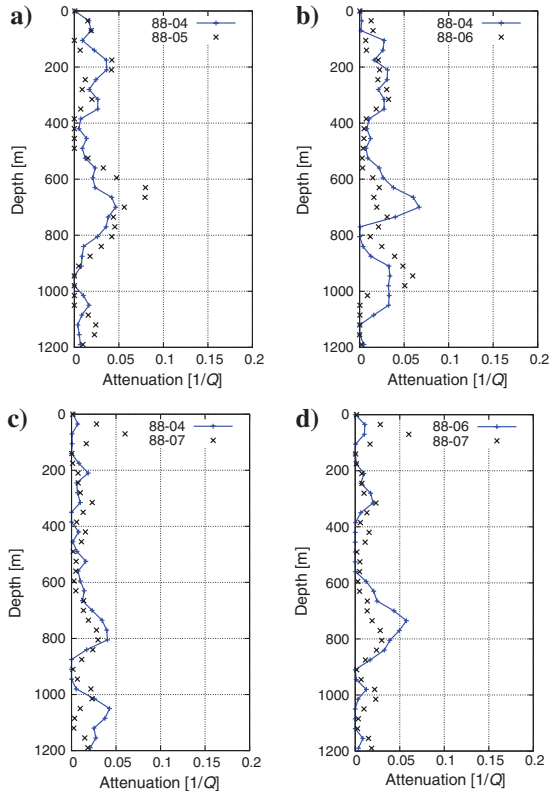

Figure 11. One-dimensional profiles of waveform tomography attenuation models at the intersection between (a) line 88-04 and line 88-05, (b) line 88-04 and line 88-06, (c) line 88-04 and line 88-07, (d) line 88-06 and line 88-07.

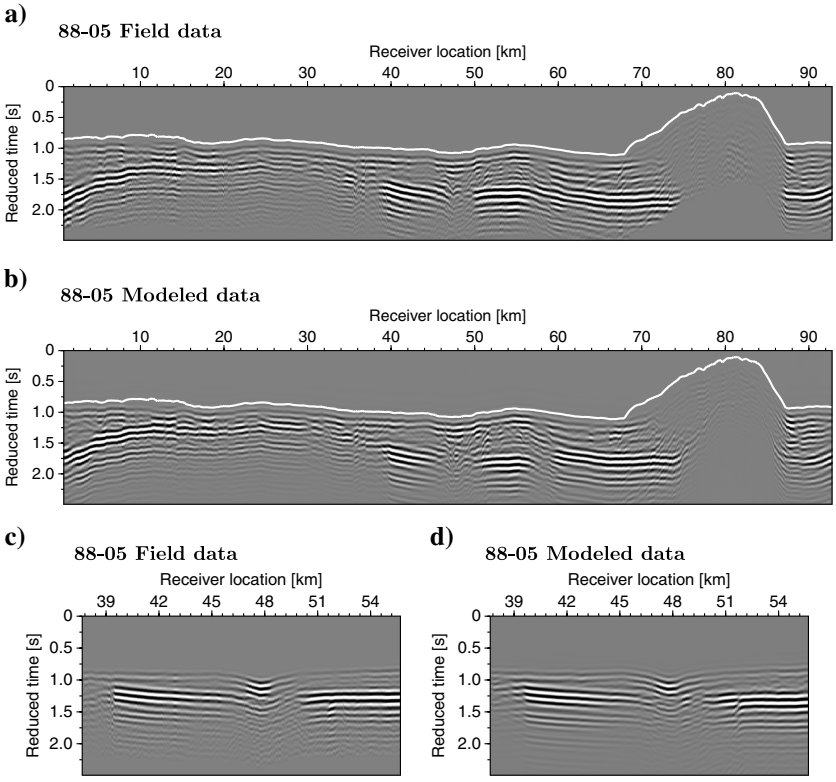

Figure 12. Line 88-05 common-offset gather (offset = 2.915 km) of (a) field data low-pass filtered to 12 Hz and (b) modeled data calculated with the velocity and attenuation models derived from the 12-Hz inversion. There is a high degree of similarity between the modeled data and the field data, within the 2-s window, mostly in the sediment, i.e., between 0–70 km and 90–95 km. (c) At offset = 2.015, the low-velocity region beneath first arrivals at 47–50 km in the field data. (d) The feature is reproduced in the modeled data. Reduction velocity $v = 5000$ ms^{-1}.

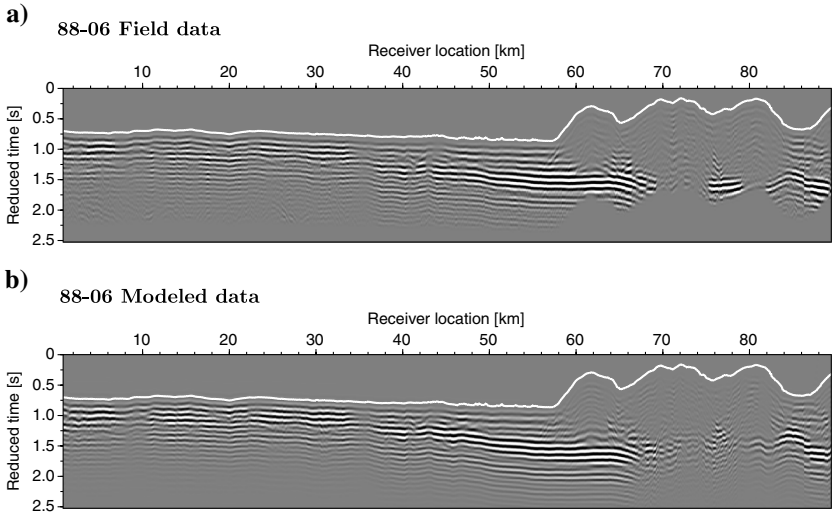

Figure 13. Line 88-06 common-offset gather (offset = 2.915 km) of (a) field data low-pass filtered to 12 Hz and (b) modeled data calculated with the velocity and attenuation models derived from the 12-Hz inversion. There is a high degree of similarity between the modeled data and the field data, within the 2-s window in the sediment, i.e., between 0 and 57 km. At the basement, i.e., between 58 and 90 km, the match is still good for the early arrivals, but poor at late times. The reduction velocity used is $v = 4000$ ms^{-1}.

shales were found in the well (Murrelet L-15 and Tyee N-39 wells). The results are compared with the estimated percentage of clay from gamma-ray logs at the respective wells using the relation of Steiber (1973) (Figure 15). It is obvious that, although the percentage of clay estimated from the gamma-ray logs is greater in places than that from the seismic attenuation values, a clear correlation exists. The peak in clay volume at 700–900 m depth at the Tyee N-39 well (Figure 15b and 15c) is relatively well resolved. Also, layers with alternating higher and lower clay content estimated from attenuation values at the Murellet L-15 well correlate consistently with the estimated clay content from the gamma-ray log (Figure 15a). It should be noted that these estimates are theoretical and that the percentage of clay estimated from the attenuation values and from the gamma-ray logs requires geological calibration. However, the correlation between the two estimates demonstrates the potential use of inverted attenuation models to estimate physical properties.

STRUCTURE AND LITHOLOGY OF THE QUEEN CHARLOTTE BASIN

In this section, we will start by reviewing the structures and faulting previously identified in the basin from migrated sections (Rohr and Dietrich, 1992; Whiticar et al., 2003). Then, we will describe the general stratigraphy and faulting of the basin, in the context of the waveform tomography models. We will use the interpretation of Rohr and Dietrich (1992) and the superposition of time-converted waveform tomography velocity models on migrated sections to interpret the shallow basin stratigraphy, which mainly includes the Pliocene and the Quaternary sections. The derived seismic attenuation will be characterized, and interpreted in terms of previous estimates for sedimentary and igneous rocks.

Seismic reflection profiles

Line 88-04

In southern Hecate Strait, line 88-04 intersects the Murrelet L-15 well, which was drilled at $x =$ 32 km (near CDP = 2008) into a deep half-graben containing up to 5.5 km of Tertiary strata (Rohr and Dietrich, 1992) (Figure 16). The half-graben bounding fault, which is located at $x = 39$ km (CDP = 2475), defines the southeast side of Moresby Ridge, a basement high comprising Mesozoic volcanic rocks and overlain by less than 500 m of Pliocene sedimentary rocks (Rohr and Dietrich, 1992). At 28–36 km (CDP = 1742–2275), the half-graben fill has

been folded and inverted into an anticline during the Late Miocene and Pliocene. At 70–105 km (CDP = 4542–6875), the extensional basin has also been inverted, resulting in a succession of faults, which have uplifted Miocene strata, e.g., at $x = 82$, 84, 88, and 96 km. Tertiary strata to the northwest are extensively disrupted by upward branching faults with various dips. Antiform A1, which is also identified on lines 88-06 and 88-07, occurs between 135 and 154 km.

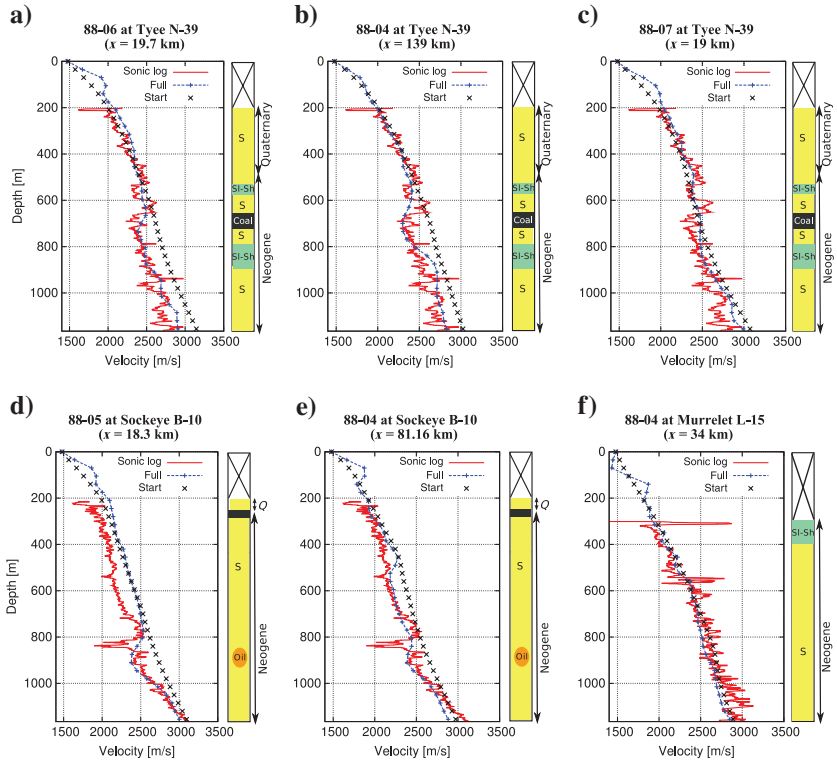

Figure 14. (a-f) Comparison of sonic logs with velocities estimated at well locations by waveform tomography. The waveform results correlate with the sonic log better than the starting model derived from traveltime tomography, and there is generally good agreement between the waveform tomography results and the sonic logs. The lithologies (S: sandstone, Sl-Si: Siltstone and shale) are derived from Shouldice (1971); Q is Quaternary.

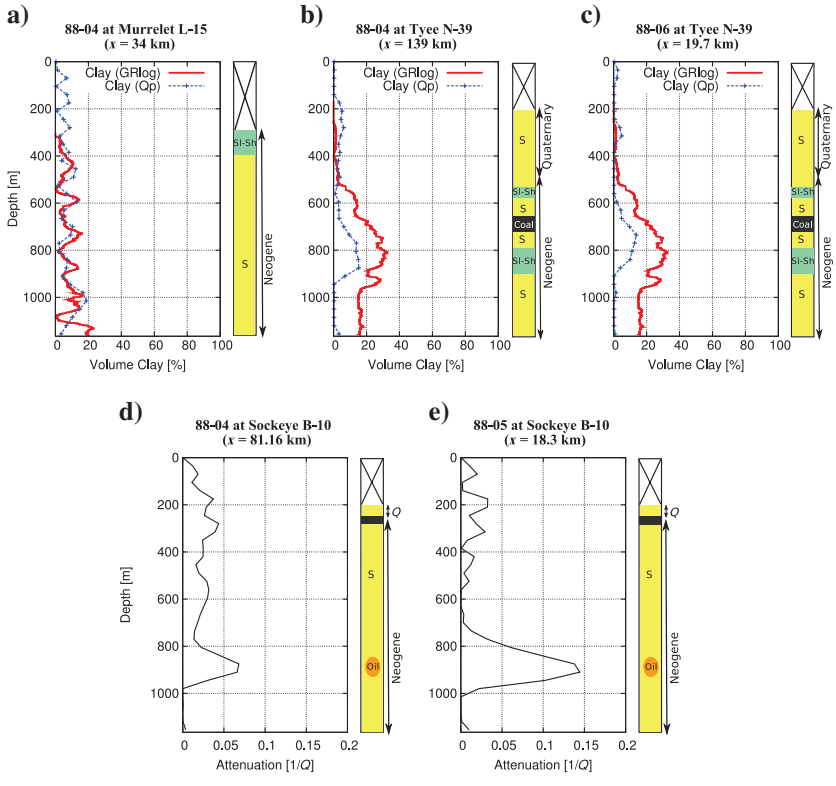

Figure 15. (a-c) Comparison of clay volume calculated from attenuation models (dotted blue) with clay volume calculated from gamma-ray logs (red). (d-e) The increase in attenuation at 800–1000 m is associated with oil staining in well. The lithologies (S: sandstone, Sl-Si: Siltstone and shale) are derived from Shouldice (1971); Q is Quaternary.

Line 88-05

At $x = 23$ km, CDP = 1408, a fault is imaged on the migrated section of line 88-05 (Figure 17). The hanging wall of this fault has been inverted into a fold, which was penetrated by the Sockeye B-10 well at location $x = 18.3$ km. An antiform, between $x = 54$–60 km, was created by inversion of the southwest part of a half-graben (CDP = 3600–4800), and is cut at $x = 60$ km (CDP = 3875) by an east-dipping fault. Between $x = 46$–78 km (CDP = 2942–5055), upper-Miocene stratigraphy thins to the northeast and onlaps the Principe-Ladero Basement High (PLBH) at $x = 79$ km. Basement rocks of the PLBH occur just beneath the seafloor from $x = 79$ km to $x = 87$ km. A steeply deeping extensional fault on the northeast margin of the PLBH marks the southwest edge of another graben. Two faults at $x = 90$ km and $x = 93$ km locally offset the graben fill.

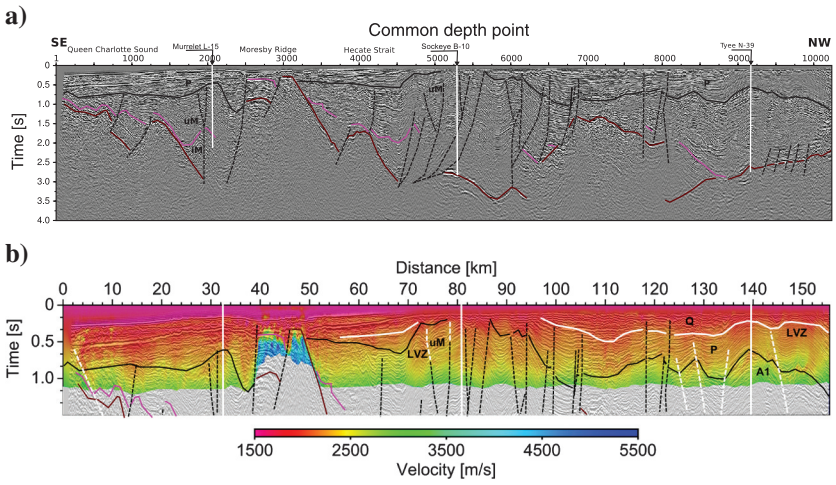

Figure 16. (a) Line 88-04 interpreted migrated seismic section Rohr and Dietrich, 1992. The black lines represent the Pliocene (P) to upper Miocene (uM) unconformity, and the black dashed lines show the location of previously interpreted faults; lM represents the lower Miocene. The white vertical line is the total extent of the well; the brown and purple lines are the top of basement and volcanic rocks, respectively. (b) The same migrated seismic section truncated at 1.5 s and superimposed on the time-converted velocity model from the 12-Hz full-waveform tomography result. The white lines show the interpreted Quaternary (Q) to Pliocene (P) unconformity and the white dashed lines indicate interpreted faults, based on waveform tomography results.

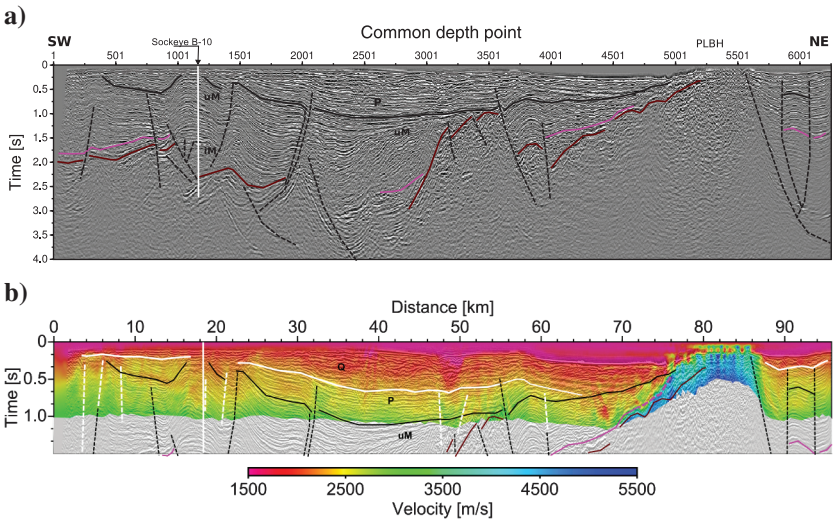

Figure 17. (a) Line 88-05 interpreted migrated seismic section (Rohr and Dietrich, 1992). The black lines represent the Pliocene (P) to upper Miocene (uM) unconformity, and the black dashed lines show the location of previously interpreted faults; lM represents the lower Miocene. The white vertical line is the total extent of the well; the brown and purple lines are the top of basement and volcanic rocks, respectively. (b) The same migrated seismic section truncated at 1.5 s and superimposed on the time-converted velocity model from the 12-Hz full-waveform tomography result. The white lines show the interpreted Quaternary (Q) to Pliocene (P) unconformity and the white dashed lines indicate interpreted faults, based on waveform tomography results.

Line 88-06

The Tyee N-39 well, which is located at $x = 19.7$ km (CDP = 1188), penetrated a faulted northwest-trending anticline, known as the Tyee structure (Rohr and Dietrich, 1992), which occurs in Miocene strata, between $x = 18$ km to $x = 35.2$ km (CDP = 1075–2222) (Figure 18). The Tyee structure is also imaged on lines 88-07 and 88-04. In the overlying Pliocene strata, the sedimentary rocks have been folded into an antiform (A1) between $x = 14.3$ km and $x = 35.2$ km (CDP = 828–2222), and also folded at $x = 11.5$ km; these strata are cut by upward branching faults as a consequence of Pliocene and Late Miocene deformation. At $x = 18$ km (CDP = 1075), a subvertical fault cuts the Pliocene rocks and delimits the Tyee structure to the west. Southwest of the Tyee structure, sedimentary rocks shoal toward Moresby Island, and are cut by vertical faults at $x = 4.5$, 5, and 9 km. Between $x = 36$ and 38.5 km (CDP = 2275–2442), a small anticline in the upper-Miocene strata with apex at $x = 37$ km (A2 in Figure 18) originated in the Miocene by shortening of a deep half-graben centered near $x = 40$ km. A small faulted anticline is present at $x = 50$–56 km. From $x = 58$ km to the end of the line, Tertiary strata thin and onlap the southwestern flank of the PLBH, where igneous basement rocks occur at depths as shallow as 250 m.

Line 88-07

Northeast of the Tyee structure imaged between $x = 10$–26 km (CDP = 542–1608), line 88-07 crosses a basement high at CDP = 3000–3501, which separates two subbasins with different structural characteristics (Figure 19). Southwest of the high, Miocene strata are unconformably overlain by flat-lying Pliocene strata. Northeast of the basement high, Miocene and Pliocene sections are folded in a broad anticline centered at $x = 66$ km (CDP = 4274) and cut by a vertical fault at $x = 63.5$ km (CDP = 4108) that offsets underlying basement rocks. Northeast of this structure, the PLBH and adjacent graben (Feeney basin) occur at CDP = 5000–7000. The Feeney basin was interpreted by Rohr and

Dietrich (1992) as a basin that may have initially formed as a graben, and was then asymmetrically uplifted and eroded. Several Miocene faults are present along the line. Pliocene deposits pinch out on basement highs between subbasins, which become shallower to the northeast, greatly reducing the thickness of the Pliocene sediments to only few tens of meters in Dixon Entrance. Line 88-07 crosses the Principe-Ladero Fault (PLF) at CDP = 7001.

Summary

In much of the basin, sedimentary strata are folded, with several anticlines present, and cut by a complex network of faults, which have created numerous Miocene subbasins that are partially inverted and unconformably overlain by Pliocene strata. To the east and north, the thickness of Pliocene sediments decreases to almost zero.

Stratigraphy and lithology from velocity models

The seafloor, whose depth was measured during the seismic survey with an acoustic echosounder, is represented in the velocity models by a fractional velocity perturbation of approximately −0.1, at x = 0–65 km, 40–95.76 km, and 50–92.79 km on lines 88-04 (Figure 5c), 88-05 (Figure 6c) and 88-06 (Figure 7c), respectively. This negative velocity perturbation may be a consequence of the acoustic waveform inversion of elastic seismic data generated by the seafloor. The inversion may accommodate the change in amplitude and phase due to mode conversion at the seafloor by slightly underestimating the velocity.

Deeper and broader, at approximately 500–600-m depth between x = 70–144 km, 10–40 km, and 4–34 km on lines 88-04 (Figure 5c), 88-05 (Figure 6c) and 88-06 (Figure 7c), respectively, the top of a fractional velocity perturbation of approximately −0.1 lies close to the previously interpreted Pliocene/upper Miocene unconformity. However, the correlation is not exact because the perturbation is also controlled by the velocity gradient of the starting model. On line 88-07, for example, there is no significant negative velocity perturbation at the Pliocene/upper Miocene unconformity at x = 0–24 km (Figures 8c and 19b) because the starting velocity gradient is close to the final model (Figure 14c). This result demonstrates the potential ambiguity that can arise from using the perturbation models for interpretation of basin stratigraphy, although horizons often appear more continuous.

At approximately 0.4–0.5 km depth, a vertical increase in velocity from 2300 ms^{-1} to 2600 ms^{-1}, which does not correlate with the deeper Pliocene/upper Miocene unconformity is observed in sedimentary rocks (x = 0–50 km) on line 88-06 (Figures 7a and 18). We interpret this increase in velocity as the Quaternary/Pliocene unconformity (Figure 18) because 450 m of Quaternary rocks were

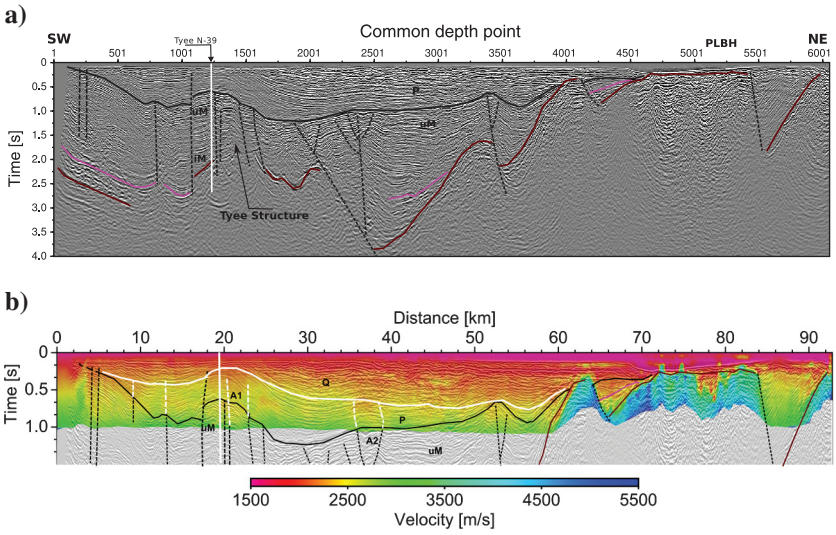

Figure 18. (a) Line 88-06 interpreted migrated seismic section (Rohr and Dietrich, 1992). The black lines represent the Pliocene (P) to upper Miocene (uM) unconformity, and the black dashed lines show the location of previously interpreted faults; lM represents the lower Miocene. The white vertical line is the total extent of the well; the brown and purple lines are the top of basement and volcanic rocks, respectively. (b) The same migrated seismic section truncated at 1.5 s and superimposed on the time-converted velocity model from the 12-Hz full-waveform tomography result. The white lines show the interpreted Quaternary (Q) to Pliocene (P) unconformity and the white dashed lines indicate interpreted faults, based on waveform tomography results. Antiforms A1 and A2 are also indicated.

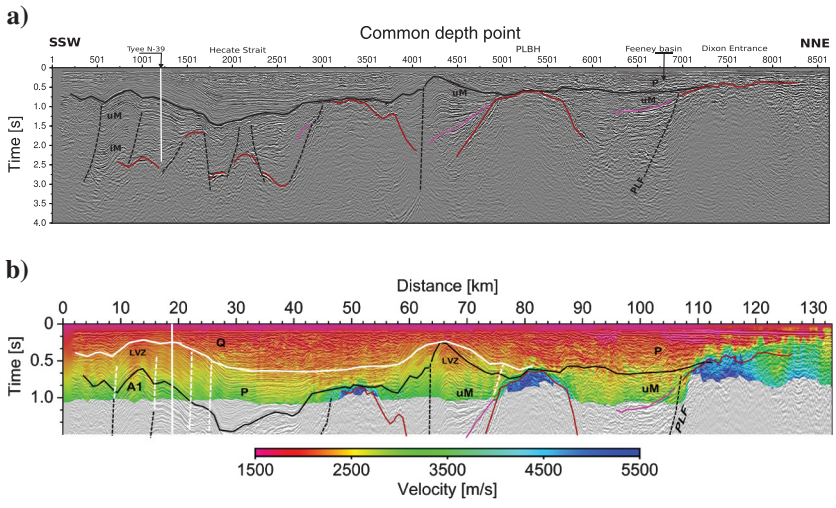

Figure 19. (a) Line 88-07 interpreted migrated seismic section Rohr and Dietrich, 1992. The black lines represent the Pliocene (P) to upper Miocene (uM) unconformity, and the black dashed lines show the location of previously interpreted faults; lM represents the lower Miocene. The white vertical line is the total extent of the well; the brown and purple lines are the top of basement and volcanic rocks, respectively. (b) The same migrated seismic section truncated at 1.5 s and superimposed on the time-converted velocity model from the 12-Hz full-waveform tomography result. The white lines show the interpreted Quaternary (Q) to Pliocene (P) unconformity and the white dashed lines indicate interpreted faults, based on waveform tomography results. LVZ are localized low-velocity zones.

identified in the Tyee N-39 well located at $x = 19.7$ km (Shouldice, 1971). Although not originally interpreted on the migrated sections, more recent work on the surficial geology of the offshore Canadian shelf, including Dixon Entrance, Hecate Strait, and Queen Charlotte Sound has identified Quaternary sediments a few hundred meters thick, underlain by Pliocene sediments (e.g., Luternauer et al., 1989; Barrie et al., 1991, 2006; Halliday et al., 2008). We also interpret the shallow increase in velocity on line 88-05 between 0 and 70 km (Figure 17a) and 88-07 between 0 and 70 km (Figure 19a) as the Quaternary/Pliocene unconformity.

Using the Pliocene/upper Miocene unconformity identified by Rohr and Dietrich (1992) and our interpretation of the Quaternary/Pliocene unconformity, it appears that Quaternary sedimentary strata are commonly characterized by velocities in the range of 1750–2300 ms^{-1}. The underlying Pliocene strata have velocities in the range of 2300–2700 ms^{-1}, and the upper Miocene strata of 2700–3000 ms^{-1}. Velocities generally increase with depth due to compaction and lithification. On line 88-04, at 0.3–0.7 km depth and between $x = 70$–105 km (Figure 16), the upper Miocene section exhibits lower velocities (2100–2800 ms^{-1}) than expected. These low velocities might be due to the abundance of faults in the region which may have increase fracturing and porosity in the sedimentary rocks and consequently reduced the velocity. The igneous basement, which is mostly Triassic, and can be identified on the migrated sections, exhibits velocities in the range 3500–5000 ms^{-1}. The high velocity at the basement might be due to volcanic or granitic rocks. However, it is not possible, using seismic velocity alone, to clearly identify the nature of these rocks because volcanic and granitic rocks have a similar velocity range. We will constrain the possible nature of these rocks using inverted attenuation models in a later section.

Subparallel sedimentary layering is evident in the velocity models: for example, on line 88-05 at $x = 47$–78 km and 87–95 km (Figure 6a and 6c), on line 88-06 at $x = 4$–36 km (Figure 7a), line 88-04 at $x = 0$–36 km and 120–134 km (Figure 5a and 5c), and line 88-07 at $x = 2$–10 km (Figure 8c), with velocities ranging between 1800 and 2300 ms^{-1} and fractional perturbation between 0.1 and 0.2. These shallow sediments are nonmarine, as shown by the exploration wells Tyee N-39, Sockeye B-10, and Murrelet L-15 (Shouldice, 1971; Rohr and Dietrich, 1992). The presence of layering suggests fairly continuous, widespread sediment deposition during the Quaternary period and the Pliocene epoch.

Interpretation of faults

Structural features identified in the velocity and velocity perturbation models might be due to faults, folds, anticlines, or synclines. Correlation of the velocity models with interpreted migrated sections suggests that subvertical sharp lateral changes in velocity are commonly related to faults (e.g., Takam et al., 2011). On all the lines, most of the upper Miocene faulting identified on the migrated sections correlates with subvertical sharp lateral decreases in velocity. We therefore interpret such changes in velocity to be due to faults. Lateral changes in the velocity perturbation of line 88-04 between 70 and 152 km, due to changes in velocity of approximately 3000–2500 ms^{-1} at 0.6 km depth, correlate with deformation observed on the migrated section (Figures 5 and 16); perturbation contrasts between −0.1 to 0.1 can be identified at $x = 74$, 78, 82, 84, 86, 96, 100, 106, 118, 123, 130, and 139 km (Figure 5c). We interpret these changes in velocity to be due to faults that correlate with previously identified faults on the migrated section. These faults result from the inversion of the extensional basin at 70–105 km, and from the formation of anticline A1 at 130–140 km (Rohr and Dietrich, 1992). Sudden northwest dipping decreases in velocity at 4 and 143 km, which do not correlate with Miocene faulting, are also interpreted as faults (Figures 5c and 16).

On line 88-06, below 0.6 km depth, lateral velocity variations in the perturbation model with values of −0.1 to −0.05 at $x = 13.5$, 18, 21, and 23 km correlate with previously identified faults in the Miocene stratigraphy (Figures 7c and 18). We interpret some lateral velocity changes in the overlaying Pliocene section as the upward continuation of these faults across the Pliocene/upper Miocene unconformity, associated with the formation of the Tyee structure. These faults cross antiform A1, and some appear to correlate with a shallow subvertical positive velocity perturbation of approximately 0.1 (Figure 7c). Usually, faults are associated with a decrease in velocity. So these subvertical features might be artifacts similar to those observed in conventional migration. Two faults, at $x = 36$ and 38.5 km, are also interpreted as the upward continuation of Miocene faulting across the unconformity, and associated with the shortening of a deep half-graben centered near 39.7 km.

On line 88-07 (Figures 8a and 19), lateral variations in velocity, at $x = 9$ and 16 km, cut antiform A1 and are interpreted, as on line 88-06, to extend upward across the Pliocene/Miocene unconformity because they correlate with Miocene faulting. Sharp lateral changes in velocity, across and close to antiform A1 at $x = 12$, 14, 22, and 26 km are also interpreted as faults. A localized steeply dipping zone of lower velocity at 77 km, which is also associated with negative fractional velocity of approximately −0.1 (Figure 8c), is interpreted as a fault.

On line 88-05, a fault, imaged on the migrated section at $x = 23$ km (CDP = 1501) (Figure 17) can also be recognized on the perturbation velocity model at $x = 23$–24 km where east-dipping sedimentary stratigraphy is disrupted by a change in the velocity perturbation image of −0.1 to 0.15 (dashed line in Figure 6c). The hanging wall and the footwall of the fault were subject to deformation and, in particular, from 0.6 km depth downward, from $x = 2$ to 30 km, east-deeping Miocene sedimentary deformation is evident on the velocity perturbation model, shown by alternating horizons with a magnitude of −0.1 to 0.1. Subvertical velocity anomalies of approximately 2500 ms^{-1}, corresponding to perturbation velocities of approximately −0.1 at $x = 4$, 6, 8, 47, and 51 km, are interpreted to be due to Pliocene faulting, and some of these faults ($x = 6$, 51 km), which correlate with previously identified faults in the Miocene, are interpreted as the extension of Miocene faults (Figure 17). Deeper, at $x = 32$ km, a sharp lateral change in velocity from 2500 ms^{-1} to 3000 ms^{-1} (Figure 6a) corresponds on the migrated section to the location of a west-dipping fault (approximately CDP = 2100). The fault at $x = 59$ km, which marks the northeast margin of a small anticline, is also interpreted to continue upward into the Pliocene section.

Seismic attenuation in sediment

Well log reports indicate that the sedimentary strata comprise clastic rocks composed mostly of sandstones with some siltstones, mudstones, clay and coal. The attenuation values recovered in these sedimentary rocks, $Q_P^{-1} \leq 0.04$ (Figures 5b, 6b, 7b, and 8b), are

generally consistent with laboratory measurements of saturated sandstone (Winker and Nur, 1979) and therefore consistent with the well logs (Figure 14). However, regions of locally elevated attenuation ($Q_P^{-1} \leq 0.06$) are identified in the sedimentary rocks and these regions appear to correlate with localized low-velocity anomalies with values of 2200–2600 ms^{-1} (Figure 9a), for example at approximately 800-m depth, between $x = 2$ and 38 km on lines 88-06 and 88-05, and at $x = 2$, 24–30, 74–102, and 112–154 km on line 88-04. Layering, with attenuation values of $Q_P^{-1} = 0.03$–0.04 is present on lines 88-06, 88-05, and mostly 88-04. However, on line 88-07, between 38 and 133 km, the sedimentary rocks with attenuation values $Q_P^{-1} = 0.03 - 0.04$ are less continuous along the line and this observation is consistent with the velocity stratigraphy (Figure 8) within the same interval. These differences in attenuation stratigraphy, may be related to a variation in the nature of sedimentary rocks, from Hecate Strait (lines 88-04, 88-05, 88-06) to southern Dixon Entrance (line 88-07). Localized zones with high-attenuation values ($Q_P^{-1} = 0.06$) along the line, for example in the Feeney basin may be due to the presence of volcaniclastic sediments.

Seismic attenuation in igneous rocks

Figures 5b, 6b, 7b, and 8b show high inverted attenuation values in the igneous basement on all lines (88-06 at $x = 62$–92.79 km, 88-05 at $x = 70 - 95.76$ km, 88-04 at $x = 0 - 40$ km, 50–155 km, and 88-07 at $x = 48 - 54$ km, 76–88 km, and 108–133 km). In these areas, there appears to be a correlation between high attenuation values ($Q_P^{-1} = 0.05$–0.15) and high velocity (≥ 3500 ms^{-1}). The recovered attenuation values may be too high in places due to elastic amplitude losses in the field data that are not included in the viscoacoustic forward modeling. Mode conversions where large physical property contrasts are present, such as at the top of igneous basement, may thus increase our estimates of attenuation because this amplitude loss can be incorporated into the attenuation. Most of the attenuation estimated for the igneous basement is in the range $Q_P^{-1} = 0.01$–0.07 (Figure 9b). These attenuation values, which correspond to low Q_P values ($Q_P = 14$–100), are consistent with laboratory measurements of intrinsic attenuation in oceanic basalts under saturated conditions and elevated pore pressure (100 MPa). The Q_P values range from eight for high porosity Lau Basin basalt to 85 for Atlantic oceanic crust (Wepfer and Christensen, 1990). Our estimated attenuation and velocity values are therefore generally consistent with volcanic rocks in the upper part of the igneous crust. This interpretation is consistent with previous geophysical studies of the Moresby Ridge, a shallow basement block in the western part of the QCB basin, where high gravity and magnetic anomalies have been interpreted to indicate the presence of Mesozoic volcanic rocks (Young, 1981), and to other related studies (Table 1). Generally, attenuation in basalt is expected to be low ($Q_P = 400$–600), but attenuation can be significantly higher where porosity is great. The high attenuation values (low Q_P) shown in Table 1 are interpreted to be due to a high porosity and alteration (Wepfer and Christensen, 1990, 1991).

DISCUSSION

Although there is generally a good correlation between velocity models derived by waveform tomography and the migrated seismic sections, we are able to identify numerous features in the velocity models that cannot be readily seen on the migrated sections. These relatively shallow features, which include shallow Pliocene faulting, affect refracted arrivals that are typically muted during conventional seismic data processing, but are included in the waveform tomography. Thus waveform tomography complements interpretations derived from conventional migrated sections. In addition, the seismic velocity of certain geological features such as the apex of antiforms can be quantified. Because viscoacoustic inversion produces estimates of velocity and attenuation in the subsurface, it is also possible to identify anomalous regions by crossplotting these two parameters (Figure 9). These anomalous regions (high attenuation associated with low velocity) correspond to geological features such as increase in clay content, seafloor pockmarks, gas chimneys, and oil staining. Below, we present these features and discuss their possible nature and origin.

Faults extending up into Pliocene

In general, many of the faults identified on the migrated sections by Rohr and Dietrich (1992) and Whiticar et al. (2003) are restricted to below the Pliocene/upper Miocene unconformity. These faults developed during the transtensional phase of basin formation, which ended in the late Miocene (Rohr and Dietrich, 1992). Using

Table 1. Intrinsic (Q_{int}) and effective (Q_{eff}) attenuation values for, respectively, laboratory experiments (Lab) using ultrasonic pulse-echo and in situ measurement of basalts using vertical seismic profile.

Locations	Data	Q_{int}	Authors
Juan de Fuca basalt	Lab	31	Wepfer and Christensen (1990, 1991)
Juan de Fuca basalt	Lab	11–17	Tompkins and Christensen (1999)
Oman Ophiolite basalt basalt	Lab	124	Wepfer and Christensen (1990, 1991)
Lau Basin basalt	Lab	8	Wepfer and Christensen (1990, 1991)
Locations	**Data**	Q_{eff}	**Authors**
Faroe lower series (Lopra)	VSP	13–24	Ker and Rodriguez (2002)
Norwegian margin (ODP hole 642E)	VSP	25	Rutledge and Winkler (1989)
Rockall Trough 164/07 – 1	VSP	15–35	Maresh et al. (2006)

the velocity models derived by waveform tomography, some of these Miocene faults are interpreted to extend shallower into the Pliocene section. These faults were identified at $x = 36$ and 38.5 km on line 88-06, across antiform A1 on lines 88-06 and 88-07 (Figures 18 and 19), and at 6 km and between 50 and 70 km on line 88-05 (Figure 17). The upward extension of these faults, into the Pliocene section, suggests that the transtensional phase of the basin formation may have ended more recently, during the Pliocene, than previously supposed.

Velocity at apex of antiforms

Typically, isovelocity contours in the derived velocity models do not follow the stratigraphy in anticlines, and velocities estimated at the apex appear to be anomalously low. A decrease in velocity of approximately 150 ms^{-1} is observed at the apex of antiform A1 at $x = 18$–23 km on line 88-06 (Figure 7a), $x =$ 16–22 km on line 88-07 (Figure 8a), and $x = 136$–148 km on line 88-04 (Figure 5a). Other decreases in velocity are observed at the apex of anticlinal folds on line 88-07 at $x = 63 - 72$ km and on line 88-06 between $x = 36$ and 38.5 km, where a sharp lateral decrease in velocity from approximately 2500 to 2300 ms^{-1} overlies a small faulted anticline in the upper-Miocene strata with its apex at $x = 37$ km (A2 in Figure 18). We interpret these decreases in velocity to be the result of tensile fractures that increase the porosity and consequently lower the velocity. Tensile fractures are probably due to folding during basin inversion; e.g., anticline A2 originated in the Miocene by shortening of a deep half-graben centered near $x = 39.7$ km (Rohr and Dietrich, 1992). Decreases in velocities at the apex of anticlinal folds have also been observed at the Cascadia accretionary wedge (Hayward and Calvert, 2007).

Porosity and oil staining in sediments

Localized low-velocity zones with velocities of 2200–2300 ms^{-1}, associated with elevated attenuation are present at 700–1000-m depth, between $x = 10$–32 km on line 88-05 (Figure 6) and at $x = 3$ km, 28–30, 74–100, 118–123 km, and 138–152 km on line 88-04 (Figure 5). Many of these zones are close to faults or folds and the low velocity and high attenuation may be due to elevated fracture porosity. However, the decrease in velocity and associated increase of attenuation on line 88-05 between $x =$ 16 and 20 km and on line 88-04 between $x = 80$ and 82 km may be linked to the oil staining identified in the Sockeye B-10 well between 950 and 1050 m. A comparison of the 1D attenuation extracted from lines 88-04 and 88-05 with the lithology log from the well (Figure 15d and 15e) shows that the strong increase in attenuation correlates with the oil staining. Elevated attenuation ($Q_P^{-1} = 0.06$–0.015) is consistent with attenuation measured in oil sandstones and gas sandstones (Klimentos, 1995). We can therefore suggest that the elevated attenuation between 8 and 20 km and at 29–34 km on line 88-05, and between 74 and 100 km on line 88-04, is due to the presence of hydrocarbons, perhaps in relatively small quantities.

Increase in clay content

An almost continuous layer of high attenuation ($Q_P^{-1} =$ 0.05–0.1), associated with localized low-velocity zones (2000–2300 ms^{-1}) at 700–900-m depth, is present between $x = 2$–35 km on line 88-06 (Figure 7). Line 88-06 intersects line 88-04 near the Tyee N-39 well and elevated attenuation associated with low-velocity zones is also present between $x =$ 136 and 140 km on line 88-04 (Figure 5) at the same depth. This layer of elevated attenuation on line 88-06 is also cut by many faults, mostly in antiform A1; so the elevated attenuation could be due to fracture porosity. However, a comparison of the percent clay content by volume calculated from the 1D Q_P-profile using equation 3 and the percent clay content calculated from the gamma-ray log at the Tyee N-39 well (Figure 15b and 15c) shows that the increase in attenuation at 700–900-m depth is associated with an increase of clay content and, over this depth range, siltstones and shale are present in the well. Therefore, we interpret the elevated attenuation between $x = 2$ and 35 km on line 88-06 and between $x = 136$ and 140 km on line 88-04 to be caused by the presence of siltstones and shale.

Seafloor pockmarks and gas chimneys

A V-shaped region of anomalously low velocity is present just below the seafloor on line 88-05 at $x = 47$–51 km. Velocities in this anomalous zone are approximately 1750–1850 ms^{-1} (Figure 6a and 6d), compared with surrounding values of 2000–2200 ms^{-1} at a depth of approximately 300 m. This anomalous zone corresponds to a chain of pockmarks in the seafloor where authigenic carbonate chimneys occur (Figure 1) (Halliday et al., 2008; Barrie et al., 2011). In the vicinity of the pockmarks, seismic arrivals are clearly delayed by the lower velocities (Figure 12). We suggest that the V-shaped low-velocity zone is the subsurface expression of hydrocarbon seepage, which has given rise to the pockmarks and carbonate chimneys with the low velocity due to the presence of gas. Authigenic carbonates are considered to be derived by microbial oxidation of hydrocarbon bearing fluids (Roberts and Aharon, 1994; Hovland et al., 2005; Wallace et al., 2006), and active venting of gas has been observed from at least 27 individual carbonate chimneys over the area (Barrie et al., 2011). Fluids may have migrated upward to the seafloor along underlying faults, which we interpret within the Pliocene section, extending to the Quaternary unconformity. Below the pockmark structure, elevated attenuation of $Q_P^{-1} = 0.05$–0.1 is present at 900–1100 m below the seafloor (Figure 6b). The high attenuation at this depth might be related to the presence of gas (Klimentos, 1995; Parra et al., 2006), but low attenuation in the overlaying sediments (200–800 m) may be due to carbonate precipitation within the clastic rocks.

At $x = 38$–40 km and deeper at $x = 67$ km on line 88-05, there are narrow, steeply dipping zones of low velocity in the range of 2100–2250 ms^{-1} that are also associated with high attenuation values: $Q_P^{-1} = 0.08$–0.1 at $x = 66$ km and $Q_P^{-1} = 0.05$–0.09 (0.09 just below the seafloor) between $x = 38$ and 40 km (Figure 6a, 6d, and 6b). These elevated attenuation values are consistent with gas sandstones or oil sandstones (Klimentos, 1995). We speculate that these features are pipe-like chimneys resulting from gas ascension. The upward migration of gas through chimneys located between $x = 38$ and 40 km and at $x = 67$ km might be responsible for the presence of a zone with relatively weak amplitude in the input data at 40–46 km (Figure 12), and a layer with elevated attenuation between $x = 62$ and 65 km at the seafloor (Figure 6b), respectively.

CONCLUSION

The Queen Charlotte basin is a complex network of half-grabens and other subbasins containing variably deformed stratigraphy. We applied viscoacoustic waveform tomography to four seismic reflection profiles that extend across the basin from Hecate Strait to Dixon Entrance. The maximum depth of penetration was restricted to 1200 m due to the 3770 m maximum offset of the input data. A carefully designed preconditioning of the data, comprising f-k filtering and amplitude corrections, and a specific inversion strategy were applied to ensure convergence to a likely global minimum. The P-wave velocity and attenuation models show a good correlation with the available sonic, gamma-ray logs, and with interpreted migrated seismic sections from previous studies. One-dimensional velocity and attenuation profiles extracted at the line intersections also show good correlation, indicating the robustness of the inversion strategy used, and synthetic data calculated from the final 12-Hz waveform tomography velocity models match the field data well.

Using velocity models from waveform tomography, it was possible to identify Quaternary strata and shallow faulting in the Pliocene section that were not interpretable on the original migrated sections. Also, some faults previously identified on the migrated section, below the Pliocene/upper Miocene unconformity, can now be extended upward into the Pliocene section. The presence of faulting in the Pliocene suggests that the transtensional phase of basin evolution continued longer than previously supposed.

P-wave velocities in sediments range between 1750 and 3000 ms^{-1} and attenuation values ($Q_P^{-1} \leq 0.04$) are generally consistent with values for saturated sandstones, but in some areas elevated attenuation ($Q_P^{-1} = 0.05$–0.15) is associated with localized low velocities (2200–2600 ms^{-1}). In basement areas, the estimated attenuation values (Q_P^{-1}) are generally between 0.01 and 0.1 and there is a correlation between high attenuation values ($Q_P = 0.05$–0.1) and high velocity ($V_P \geq 3500$ ms^{-1}). These rocks are interpreted to be volcanic, but the elevated effective attenuation could also be an artifact due to scattering or mode conversion effects, which are not included in the inversion.

Decreases in velocity of approximately 150 ms^{-1} at the apex of anticlinal folds were observed on lines 88-06, 88-04, and 88-07 and are interpreted to be due to tensile fracturing that increases the porosity and consequently lowers the seismic velocity. Elevated attenuation, associated with localized low-velocity zones are present deeper on lines 88-04, 88-05, and 88-06 (at 700–1000-m depth), and are close to the location of faults and folds. These regions with elevated attenuation and localized low velocities may be due to fracture related porosity. However, the correlation of high attenuation with greater clay content and the presence of siltstones and shale in the Tyee N-39 well at 700-m depth, suggest that elevated attenuation at 2–36 km on line 88-06 and 136–140 km on line 88-04 is related to the presence of siltstones and shale. High attenuation, associated with anomalously low-velocity zones was also found at the Sockeye B-10 well location on lines 88-05 and 88-04, and in this case, correlates with the occurrence of oil staining in the well at 950–1050-m depth.

A shallow V-shape low-velocity anomaly was identified on line 88-05 immediately beneath a chain of seafloor pockmarks, where authigenic carbonate chimneys, which are interpreted to be related to hydrocarbon seepage, occur. West of the V-shape anomaly at $x =$ 38–40 km and deeper at $x = 67$ km on line 88-05, subvertical zones of low velocity associated with high attenuation values are interpreted as pipe-like chimneys resulting from gas ascension.

ACKNOWLEDGMENTS

We are grateful to Gerhard Pratt, who provided us with his waveform tomography code. Well logs from the Tyee N-39, Sockeye B-10, and Murrelet L-15 were provided by Divestco. The seismic data were plotted with SeimicUnix and Gnuplot. SeismicUnix was also used partially to process the data. This project was funded by the Natural Sciences and Engineering Research Council of Canada. The final manuscript was improved by comments from Ian Jones, Elive Menyoli, and two anonymous reviewers.

REFERENCES

Aldridge, D. F., and D. Oldenburg, 1993, Two-dimensional tomographic inversion with finite-difference traveltimes: Journal of Seismic Exploration, **2**, 257–274.

Barnes, C., and M. Charara, 2008, Full-waveform inversion results when using acoustic approximation instead of elastic medium: 78th Annual International Meeting, SEG, Expanded Abstracts, 1895–1899.

Barrie, J., K. Conway, H. Josenhans, J. Clague, R. Mathewes, and D. Fedje, 2006, Late quaternary geology of Haida Gwaii and surrounding marine areas, *in* D. W. Fedje, and R. W. Mathewes, eds., Haida Gwaii: Human history the time of loon to the time of iron people: UBC Press, 1–20.

Barrie, J. V., B. Bornhold, K. C. and, and J. L. Luternauer, 1991, Surficial geology of the northwestern Canadian continental shelf: Continental Shelf Research, **11**, 701–715, doi: 10.1016/0278-4343(91)90075-H.

Barrie, J. V., S. Cook, and K. W. Conway, 2011, Cold seeps and benthic habitat on the Pacific margin of Canada: Continental Shelf Research, **31**, S85–S92, doi: 10.1016/j.csr.2010.02.013.

Brossier, R., S. Operto, and J. Virieux, 2009, Two-dimensional seismic imaging of the Valhall model from synthetic OBC data by frequency-domain elastic full-waveform inversion: 79th Annual International Meeting, SEG, Expanded Abstracts, 2293–2297.

Dietrich, J. R., 1995, Petroleum resource potential of the Queen Charlotte Basin and environs, west coast Canada: Bulletin of Canadian Petroleum Geology, **43**, 20–34.

Halliday, E., J. Barrie, N. Chapman, and K. Rohr, 2008, Structurally controlled hydrocarbon seeps on a glaciated continental margin, Hecate Strait, offshore British Columbia: Marine Geology, **252**, 193–206, doi: 10.1016/j.margeo.2008.04.009.

Hayward, N., and A. Calvert, 2007, Seismic reflection and tomographic velocity model constraints on the evolution of the Tofino forearc basin, British Columbia: Geophysical Journal International, **168**, 634–646, doi: 10.1111/gji.2007.168.issue-2.

Higgs, R., 1991, Sedimentology, basin-fill architecture and petroleum geology of the Tertiary Queen Charlotte Basin, British Columbia, *in* G. Woodsworth, ed., Evolution and hydrocarbon potential of the Queen Charlotte Basin, British Columbia: Geological Survey of Canada, **90–10**, 337–371.

Hovland, M., H. Svensen, C. F. Forsberg, H. Johansen, C. Fichler, J. H. Fosså, R. Jonsson, and H. Rueslåtten, 2005, Complex pockmarks with carbonate-ridges off mid-Norway: Products of sediment degassing: Marine Geology, **218**, 191–206, doi: 10.1016/j.margeo.2005.04.005.

Irving, E., A. J. Bakera, P. J. Wynnea, T. S. Hamilton, and M. T. D. Wingatec, 2000, Evolution of the Queen Charlotte Basin; Further paleomagnetic evidence of Tertiary extension and tilting: Tectonophysics, **326**, 1–22, doi: 10.1016/S0040-1951(00)00143-8.

Ker, S., and S. Rodriguez, 2002, Seismic properties of the Faroe basalt formations: The LOPRA-1 VSP case study: Journal of Conference Abstracts, **7**, no. 2, 158–159.

Klimentos, T., 1995, Attenuation of P- and S-waves as a method of distinguishing gas and condensate from oil and water: Geophysics, **60**, 447–458, doi: 10.1190/1.1443782.

Klimentos, T., and C. McCann, 1990, Relationships among compressional wave attenuation, porosity, clay content, and permeability in sandstones: Geophysics, **55**, 998–1024, doi: 10.1190/1.1442928.

Lewis, T. J., W. H. Bentkowski, and J. A. Wright, 1991, Thermal state of the Queen Charlotte Basin, British Columbia: Warm, *in* G. J. Woodsworth, ed., Evolution and hydrocarbon potential of the Queen Charlotte Basin: Geological Survey of Canada, **90–10**, 489–506.

Luternauer, J. L., K. W. Conway, J. J. Clague, and B. Blaise, 1989, Late Quaternary geology and geochronology of the central continental shelf of western Canada: Marine Geology, **89**, 57–68, doi: 10.1016/0025-3227(89)90027-3.

Lyatsky, H., 1993, Basement-controlled structure and evolution of the Queen Charlotte Basin, west coast of Canada: Tectonophysics, **228**, 123–140, doi: 10.1016/0040-1951(93)90217-8.

Mallick, S., and N. L. Fraser, 1987, Practical aspect of reflectivity modeling: Geophysics, **52**, 1355–1364, doi: 10.1190/1.1442248.

Maresh, J., R. S. White, R. W. Hobbs, and J. R. Smallwood, 2006, Seismic attenuation of Atlantic margin basalts: Observations and modeling: Geophysics, **71**, no. 6, B211–B221, doi: 10.1190/1.2335875.

Parra, J. O., C. L. Hackert, P.-C. Xu, and H. A. Collier, 2006, Attenuation analysis of acoustic waveforms in a borehole intercepted by a sand-shale sequence reservoir: The Leading Edge, **25**, 186–193, doi: 10.1190/1.2172311.

Pratt, R. G., 1999, Seismic waveform inversion in the frequency domain, Part 1: Theory and verification in a physical scale model: Geophysics, **64**, 888–901, doi: 10.1190/1.1444597.

Pratt, R., 2008, Waveform tomography — Successes, cautionary tales, and future directions: 70th Conference and International Exhibition, EAGE, Extended Abstracts, WO11.

Pratt, R., F. Hou, K. Bauer, and M. H. Weber, 2004, Waveform tomography images of velocity and inelastic attenuation from the Mallik 2002 crosshole seismic surveys , *in* S. R. Dallimore, and T. S. Collet, eds., Scientific results from the Mallik 2002 gas hydrate production research well program, Mackenzie delta, Northwest Territories, Canada: Geological Survey of Canada, **545**, 14.

Pratt, R. G., C. Shin, and G. J. Hicks, 1998, Gauss-Newton and full Newton methods in frequency space seismic waveform inversion: Geophysical Journal International, **133**, 341–362, doi: 10.1046/j.1365-246X.1998.00498.x.

Pratt, R., and R. Shipp, 1999, Seismic waveform inversion in the frequency domain, Part 2: Fault delineation in sediments using crosshole data: Geophysics, **64**, 902–914, doi: 10.1190/1.1444598.

Roberts, H. H., and P. Aharon, 1994, Hydrrocarbon-derived carbonate buildups of the northern gulf of Mexico continental slope: A review of submersible investigations: Geo-Marine Letters, **14**, 135–148, doi: 10.1007/BF01203725.

Rohr, M. M. K., and R. J. Dietrich, 1992, Strike-slip tectonics and development of the Tertiary Queen Charlotte Basin, offshore western Canada: Evidence from seismic reflection: Basin Research, **4**, 1–20.

Rutledge, J. T., and H. Winkler, 1989, Attenuation measurements from vertical seismic profile data: Leg 104, site 642, *in* O. Eldholm, J. Thiede, and E. Taylor, eds.: Proceedings of the Ocean Drilling Program: Scientific Results: Ocean Drilling Program, **104**, 965–972.

Shouldice, D. H., 1971, Geology of the western Canadian continental shelf: Bulletin of Canadian Petroleum Geology, **19**, 405–436.

Sirgue, L., 2003, Inversion de la forme d'onde dans le domaine fréquentiel de données sismiques grands offsets: Ph.D. thesis, École Normale Supérieure de Paris.

Sirgue, L., and R. G. Pratt, 2003, Waveform inversion under realistic conditions: Mitigation of non-linearity: 73rd Annual International Meeting, Expanded Abstracts, 694–697.

Sirgue, L., and R. G. Pratt, 2004, Efficient waveform inversion and imaging: A strategy for selecting temporal frequencies: Geophysics, **69**, 231–248, doi: 10.1190/1.1649391.

Steiber, R. G., 1973, Optimization of shale volumes in open hole logs: Journal of Petroleum Technology, **31**, 147–162.

Takam Takougang, E. M., and A. J. Calvert, 2010, Waveform tomography strategy for seismic reflection data from the Queen Charlotte Basin of western Canada: 80th Annual International Meeting, SEG, Expanded Abstracts, 4269–4274.

Takam Takougang, E. M., and A. J. Calvert, 2011, Application of waveform tomography to marine seismic reflection data from the Queen Charlotte Basin of western Canada: Geophysics, **76**, no. 2, B1–B16, doi: 10.1190/1.3553478.

Tompkins, M. J., and N. Christensen, 1999, Effects of pore pressure on compressional wave attenuation in a young oceanic basalt: Geophysical Research Letters, **26**, 1321–1324, doi: 10.1029/1999GL900216.

Van der Heyden, P., 1992, A middle Jurassic to early Tertiary Andean-Sierran arc model for the coast belt of British Columbia: Tectonophysics, **173**, 163–174.

Wallace, P., M. Harrington, and R. Cook, 2006, Carbonate blocks found in muddy sediment off Cape Breton Island, Nova Scotia: Pieces of small authigenic carbonate mounds and vents related hydrocarbon seeps: Atlantic Geology, **42**, 127–137.

Wepfer, W. W., and N. L. Christensen, 1990, Compressional wave attenuation in oceanic basalts: Journal of Geophysical Research, **95**, 17431–17439, doi: 10.1029/JB095iB11p17431.

Wepfer, W. W., and N. L. Christensen, 1991, Q structure of the oceanic crust: Marine Geophysical Researches, **13**, 227–237, doi: 10.1007/BF00369151.

Whiticar, M., T. Schuemann, and K. Rorh, 2003, Analysis of petroleum potential in Queen Charlotte Basin, Phase I: Technical report: University of Victoria.

Winker, K., and A. Nur, 1979, Pore fluids and seismic attenuation in rocks: Geophysical Research Letters, **6**, 1–4, doi: 10.1029/GL006i001p00001.

Woodsworth, G., 1991, Evolution of hydrocarbon potential of the Queen Charlotte Basin, British Columbia: Geological Survey of Canada, **90-10**, 569.

Young, L. F., 1981, Structure of the western margin of the queen charlotte basin, British Columbia: M.S. thesis, University of British Columbia.